© 2019 by Courtney Krafczyk. All rights reserved.

INVESTIGATIONS OF QUANTUM SENSING TECHNIQUES FOR DEFLECTION AND DISPLACEMENT METROLOGY

BY

COURTNEY KRAFCZYK

DISSERTATION

Submitted in partial fulfillment of the requirements
for the degree of Doctor of Philosophy in Physics
in the Graduate College of the
University of Illinois at Urbana-Champaign, 2019

Urbana, Illinois

Doctoral Committee:

Professor S. Lance Cooper, Chair
Professor Paul G. Kwiat, Director of Research
Associate Professor Virginia Lorenz
Associate Professor Smitha Vishveshwara

Abstract

We discuss our effort toward designing experiments to surpass the standard quantum limit in deflection and displacement measurements. First, we review weak measurements techniques, then describe our strategy and results from implementing recycling to measure a beam deflection. We then discuss how spatial correlations emerge from spontaneous parametric downconversion and how we utilize those correlations to improve the achievable resolution of a beam displacement. Finally, we discuss a possible way to use a quantum eraser to improve the signal from an atomic force microscope.

To Vera and my babies who don't exist just yet.

I hope you find something to love, something to do when you feel like giving up.

Acknowledgments

On my first day in my first lab, my first advisor, Professor Mendes, told me, "If I had known everything I knew at the end of my PhD at the beginning, I could have done it in 3 months. But I didn't, so it took me 5 years." I think he must have been very efficient, because my graduate school journey took 8 years. Lucky for me, in my time I've surrounded by many people who supported and made my experience a treasure.

Thank you to my advisor, Paul Kwiat, for opening the door to quantum optics, and for his guidance throughout this work. Thank you to our theorist collaborators, Andrew Jordan and his students Justin Dressel and Kevin Lyons, who were reliable and patient in working out several kinks in the weak measurement experiments. Thank you to Mike Goggin, for his calming influence and for noticing some key mistakes that allowed me to finished the recycled weak measurements experiment properly. Thank you to Lance Cooper, for his calming influence and for contributing to the close-knit culture of the physics department. Thank you to the staff of the physics department, especially Betsy Greifenkamp, Cheryl Sabas, and Wendy Wimmer, who help make Loomis a lovely place to work and who seamlessly keep the administrative ball rolling.

Thank you to Sergio Mendes, for having confidence in me when I didn't have confidence in myself, and for showing me that I could be a scientist if I wanted to be.

Thank you to Soyoung Baek, for getting the SPDC experiment up and running, and for being a trusty friend and mentor. Thank you to Aditya Sharma, who made the SPDC experiment possible. He returned at a dark point in my career, and helped remind me why I enjoy experimental science.

Thank you to my labmates, who made a collaborative, welcoming, invigoriating environment in which to work. Thanks to Han Xue, Jennifer Burnett, Soyoung Baek, Rebecca Holmes, Brianne Gutmann, Tanya Perlova, Michelle Victora, and Kristina Meier for being my scientific sisters and always having my back. A special thanks to Trent Graham, who was my mentor from my first day in my new lab.

Thank you to the Carle midwifery team, especially Sarah Procko and Carissa Swiatek, who showed me that the most impactful science isn't always done in a lab.

And thank you to my partner, Matthew Krafczyk, for being my foundation. He kept me going when I wanted to quit.

Table of Contents

List of Abbreviations

AAV	Aharonov, Albert, and Vaidman
AFM	atomic force microscope
APD	avalanche photodiode
BS	beamsplitter
CW	clockwise
CCW	counter-clockwise
H	horizontal polarization
HWP	half-wave plate
PBS	polarizing beamsplitter
PC	Pockels cell
QE	quantum eraser
SBC	Soleil-Babinet compensator
SNR	signal-to-noise ratio
SPDC	spontaneous parametric downconversion
SQL	standard quantum limit
V	vertical polarization
WM	weak measurement
WP	waveplate
WV	weak value

Chapter 1

Introduction

Optics in the modern age has brought about some beautifully precise measurements through understanding and manipulating the quantum properties of light. To name a few, perhaps most famously, the LIGO experiment observed a 10^{-18} m change in space from gravitational waves caused by two black holes colliding 10^{25} m from Earth [1]. Recently, IBM researchers demonstrated a single-electron current meter using an atomic force microscope [2], which bounces light from the end of a cantilever to measure its position. Researchers at the University of Rochester were able to measure a tilt in the angle of a mirror caused by shifting one end of it by a distance equivalent to the nucleus of a uranium atom [3] - an experiment we will revisit later. All these experiments, and any experiment utilizing light as a detector, are ultimately limited by the quantum nature of light.

The research presented here investigates how to use a quantum-optics toolbox to make measurements more precisely than the standard quantum limit (SQL). The SQL is the minimum uncertainty one can expect from a measurement using laser light - the most 'standard' resource in an optics lab. Let us consider the uncertainty in a measurement of the phase between two laser beams, a ubiquitous technique used in many experiments. (The following is adapted from [4]). We start with a well known expression: the Heisenberg uncertainty relation for energy and time

$$\Delta E \Delta t \geq \frac{\hbar}{2}. \tag{1.1}$$

E is related directly to the number of measured photons by $E = \hbar\omega N$, and t is directly related to the phase by $\phi = \omega t$. Replacing E and t with N and ϕ in Eqn. (1.1) gives

$$\Delta\phi\Delta N \geq \frac{1}{2} \implies \Delta\phi \geq \frac{1}{2\Delta N}. \tag{1.2}$$

In other words, the uncertainty in the phase is inversely proportional to the uncertainty in the number of photons. Lasers function by storing many photons in a resonant cavity with a gain medium, while a small percentage leak out through a partially transmitting mirror. This leakage occurs randomly and

independently for each photon, which tells us the photon number will be Poisson distributed, or $\Delta N = \sqrt{N}$ (a fact famously proven by Glauber [5] in his landmark description of coherent states)[1]. That gives us the SQL

$$\Delta\phi = \frac{1}{2\sqrt{N}}. \tag{1.3}$$

Eqn. (1.1) implies that the uncertainty in ϕ can be changed and controlled by choosing a different state of light, whose variance might be different than $\sqrt{N}$. One may naturally wonder: what is the largest one could make ΔN, so $\Delta\phi$ is the smallest? Well, intuitively its hard to imagine fluctuations in the average number being larger than the average number, so it is not too hard to imagine that $\Delta N = N$ is the best one can do. In that case, the uncertainty in the phase would be

$$\Delta\phi = \frac{1}{2N}. \tag{1.4}$$

This is referred to as the 'Heisenberg limit', as the Heisenberg uncertainty relation is saturated. In fact, it is theoretically possible to achieve the Heisenberg limit for metrology with particular states known as N00N states [6]. N00N states are a superposition of a large number of photons being all in one state or another, $\frac{|N0\rangle+|0N\rangle}{\sqrt{2}}$, and thus the photon number is maximally unknown.

Like most things that sound too good to be true, there is a catch that prevents most experiments with N00N states from achieving the Heisenberg limit except when using one or two photons - they are exponentially sensitive to loss, and for any significant number of photons actually perform *worse* than coherent states for realistic losses. Some states, called squeezed states [7], can perform somewhere between the SQL and the Heisenberg limit, though typically closer to the latter than the former [8]. In our research, we sought to achieve sensitivities below the SQL without using exotic quantum states. We explored various schemes to beat the SQL by a factor, though we remained limited to $\frac{1}{\sqrt{N}}$ scaling. We have chosen to focus this research on measuring the displacement of beams instead of the phase, but the same rules apply. In Chapters 2 and 3 we will discuss weak measurements (a classical phenomenon that is none-the-less ubiqutious in the quantum optics community). In Chapters 4 and 5 we review our work using spatial correlations from spontaneous parametric downconversion to demonstrate significant improvements over the achievable resolution of classically uncorrelated light. Finally, in Chapter 6 we examine an attempt to use a quantum eraser to improve the sensitivity of atomic force microscopes, before concluding in Chapter 7 with a summary

[1] We can also readily show that laser light is Poisson distributed from a quantum description of a coherent state, $|\alpha\rangle = \exp\frac{-|\alpha|^2}{2}\sum_N \frac{\alpha^N}{\sqrt{N!}}|N\rangle \implies |\langle N|\alpha\rangle|^2 = \exp -|\alpha|^2 \frac{\alpha^{2N}}{N!}$. which is a Poisson distribution with average number $N = |\alpha|^2$ and variance $= N$.

of our work.

Chapter 2

Weak Measurements

2.1 An Introduction to Weak Measurements

Aharonov, Albert, and Vaidman (AAV) caused quite a stir when they first introduced the idea of a weak measurement (WM) in their 1988 paper titled 'How the result of a measurement of a component of the spin of a spin-1/2 particle can turn out to be 100' [9], in which they detailed using an unusual setup of a Stern-Gerlach device to apparently measure an electron with a spin of 100 (see Fig 2.1).

Before discussing the validity of their sensational claim, let us consider how the spin of an electron would be determined in a conventional measurement. A Stern-Gerlach apparatus, the canonical experiment used to measure electron spin, is shown in Fig.2.1(a). A beam of charged particles with spin aligned in the x-direction travel in the y-direction and encounter a magnetic field oriented along z. Since spin along x is an equal superposition of spin along $+z$ and $-z$, if the magnetic field varies along z, it will separate (depending on the strength of the field) into two beams deflected upward or downward.[1] The spin of the particles could be determined by measuring the distance between the peaks of the two deflected beams after propagating

[1]The combination of charge and spin give each particle a magnetic moment $\overrightarrow{\mu}$, so each has an energy $-\overrightarrow{\mu}\cdot\overrightarrow{B}$ in the presence of a magnetic field $\overrightarrow{B}$. The field causes a force $F_z = \frac{dU}{dz} = -\frac{d}{dz}(\overrightarrow{\mu}\cdot\overrightarrow{B}) = \mu_z\frac{dB_z}{dz}$. Because the spin is quantized, the particle is deflected either up or down.

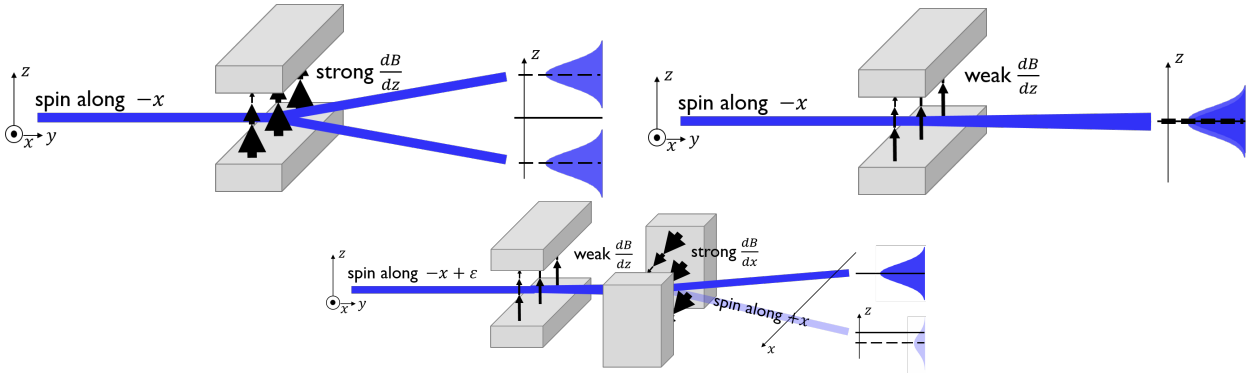

Figure 2.1: A conventional measurement of electron spin with (a) a strong magnetic field gradient and (b) a weak magnetic field gradient. (c) A weak measurement of electron spin.

some distance. If the field gradient is too weak and/or the interaction region too short, the deflection of the particles could be much less than the momentum uncertainty, making it seemingly impossible to detect, as in Fig. 2.1(b).

AAV imagined instead a beam of electrons with a Gaussian position distribution spin-polarized nearly along the -x-direction (so, in the $(-x+\epsilon)$-direction) entering a region with a small magnetic field gradient pointing along the z-direction, as in a typical Stern-Gerlach experiment. The scandalous observation came from adding another Stern-Gerlach setup after the first, in which they imagined applying a large magnetic field gradient along the x-direction to separate the beam into another two bunches; one deflected along $-x$ containing most of the electrons, and another along $+x$ with few electrons (from the fact that the beam was initially $(-x+\epsilon)$ polarized).

AAV showed that if one examined the 2D position distribution of the $-x$-deflected electrons, she would find the center of that distribution in the z-direction to be shifted much farther than in the case of the typical Stern-Gerlach experiment. From this, they claimed that one could conclude that the average spin of the $-x$-deflected electrons was 100.

More generally, they called the anomalously large result a 'weak value' (WV), and derived it as follows (though, it is easier to follow in [10]); a system is described by the wavefunction

$$|\Psi\rangle = |\psi_{met}\rangle\,|\phi_{sys}\rangle = \int \psi(x)\,|x\rangle\,dx\,|\phi_i\rangle \tag{2.1}$$

where $|\psi_{met}\rangle = \int \psi(x)\,|x\rangle\,dx$ is the wavefunction of the meter, $|\phi_i\rangle = \sum_j c_j\,|a_j\rangle$ is the input system state, and $|a_j\rangle$ are the basis states. The system and meter are then coupled through the evolution operator $U = e^{-ixA}$, resulting in the state

$$|\Psi\rangle = \int e^{-ixA}\psi(x)\,|x\rangle\,|\phi_i\rangle\,dx \approx \int (1-ixA)\psi(x)\,|x\rangle\,|\phi_i\rangle\,dx. \tag{2.2}$$

Finally, a measurement is made by projection onto a final state, $|\phi_f\rangle = \sum_j c'_j\,|a_j\rangle$, resulting in

$$\langle\phi_f|\,U\,|\Psi\rangle = \int \psi(x)\,|x\rangle\,\langle\phi_f|\phi_i\rangle\,dx - i\int x\psi(x)\,|x\rangle\,\langle\phi_f|\,A\,|\phi_i\rangle\,dx. \tag{2.3}$$

Renormalizing gives

$$\frac{\langle\phi_f|\,U\,|\Psi\rangle}{\langle\phi_f|\phi_i\rangle} = \int \psi(x)\,|x\rangle\,dx - i\int x\psi(x)\,|x\rangle\,\frac{\langle\phi_f|\,A\,|\phi_i\rangle}{\langle\phi_f|\phi_i\rangle}dx \tag{2.4}$$

$$= \int \psi(x) \left|x\right\rangle dx - i \int x\psi(x) \left|x\right\rangle A_w dx$$

where

$$A_w = \frac{\langle \phi_f | A | \phi_i \rangle}{\langle \phi_f | \phi_i \rangle} \tag{2.5}$$

is the famous weak value. If the second term is much smaller than the first, we can approximate this as

$$\int \psi(x) e^{-ixA_w} \left|x\right\rangle dx. \tag{2.6}$$

This would appear in the conjugate basis as

$$\int \psi(k - A_w) \left|k\right\rangle dk, \tag{2.7}$$

which is a displacement in the momentum distribution. Note that if the initial and final states of the system, $|\phi_i\rangle$ and $|\phi_f\rangle$, are nearly orthogonal, the WV can be arbitrarily large.

In the case of the Stern-Gerlach experiment, A is the spin operator, σ_z, $|\psi_{met}\rangle$ is the position state of the electrons, which they assumed was Gaussian, and $|\phi_{sys}\rangle$ is the spin polarization of the electrons. Initially the electrons have spins nearly along the (-x+ϵ)-direction, which they wrote as

$$|\phi_i\rangle = \cos\frac{\alpha}{2}|\uparrow_x\rangle + \sin\frac{\alpha}{2}|\downarrow_x\rangle = (\cos\frac{\alpha}{2} + \sin\frac{\alpha}{2})|\uparrow_z\rangle + (\cos\frac{\alpha}{2} - \sin\frac{\alpha}{2})|\downarrow_z\rangle, \tag{2.8}$$

where α is the angle between the spin and the x axis. Finally, only $+x$-aligned electrons are examined, so

$$\langle \phi_f | = \langle \uparrow_x | = \frac{1}{\sqrt{2}}(\langle \uparrow_z | + \langle \downarrow_z |) \tag{2.9}$$

From this, one can find the WV of σ_z to be $\tan\frac{\alpha}{2}$. If $\alpha = 178.8°$, one might conclude from this experiment that the spin was 100!

It was quickly pointed out [11] that while it was not technically invalid to conclude that the electrons in the measured distribution *behaved as if* they had spin 100, it was more consistent with generally accepted theory to say that the electrons had spin 1/2 and a subset with an unusually large average position were postselected by virtue of the set-up... which is not the usual interpretation of a 'measurement'.

AAV's opaque yet dramatic description was made more clear and less unsettling by Duck, Stevenson, and Sudarshan [12] the following year. They showed that a WM is most easily understood as destructive

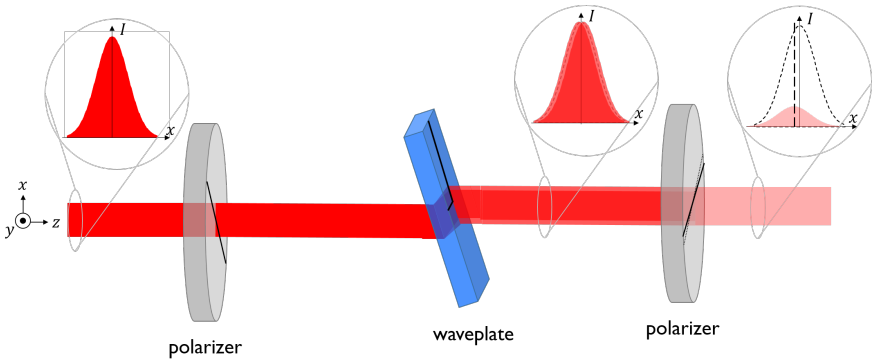

Figure 2.2: The first optical implementation of a weak measurement [13]. D-polarized light passes through a tilted waveplate with axes oriented along H and V, causing a superposition of the two with a small relative lateral shift. An (A+ϵ) polarizer postselects light and the transmitted spatial distribution is measured.

interference between the complex probability position-amplitudes of the slightly shifted spin-up and spin-down electrons. The anomalously large value is only observed when A_w is much smaller than the spread in the position distribution. Their explanation is demonstrated more clearly in the next section.

2.2 A Modern Understanding of Weak Measurements

In the years since AAV's publication, the quantum optics community has developed a more straight-forward understanding of WV and WM. See [10] for a nice summary. A WM, as discussed above, is an interferometric phenomenon. It is performed in 3 steps: preselection, weak interaction, and postselection. Preselection involves setting up an interferometer in some initial state, typically such that particles are split 50/50 between two states. Next, a weak interaction slightly disturbs the two states, providing a small amount of which-state coupling to another degree-of-freedom (frequently, position). Finally, a postselection is done by interfering the two states such that any input particles are unlikely to be measured at all, then examining the disturbed degree-of-freedom to determine the strength of the weak interaction. The WV, from Eqn. (2.5), is the expected average outcome of the interaction, given the preselected and postselected states.

Duck et al. [12] proposed an easy-to-understand-and-implement optical version of the spin experiment that perfectly illustrates the preselection, weak interaction, and postselection. It was demonstrated by Ritchie et al. [13]. Their setup, the first-ever WM (Fig. 2.2), used a polarization interferometer to measure an anomalously large shift in the transverse position of two beams from tilting a piece of quartz.

First, a Gaussian beam was polarized along the diagonal (D) direction, creating the electric field

$$E_{in} = [\cos\alpha|H\rangle + \sin\alpha|V\rangle] \exp(\frac{-x^2}{4\sigma^2}) \tag{2.10}$$

where $\alpha = \frac{\pi}{4}$. This is the preselection; note that there are two interferometer paths determined by the polarization. The beam was then passed through a crystalline quartz waveplate (WP) oriented so that the horizontal (H) and vertical (V) components of the electric field aligned with the ordinary and extraordinary axes of the crystal, meaning that H and V experience different indices of refraction. The WP was tilted in the y-direction causing the H and V polarizations to be deflected by different amounts inside the crystal, therefore causing the two to be slightly displaced relative to one another after exiting the crystal, resulting in the following electric field:

$$E_{wp} = \cos\alpha e^{i\phi} \exp(\frac{-(x+\frac{a}{2})^2}{4\sigma^2})|H\rangle + \sin\alpha \exp(\frac{-(x-\frac{a}{2})^2}{4\sigma^2})|V\rangle \tag{2.11}$$

where a is the relative displacement determined by Snell's law and ϕ is a relative phase coming from the different optical path lengths in the crystal. This is the weak interaction. The state was disturbed by an amount a, which must be small compared to σ in order for the WV to be an appropriate approximation. Finally, a polarizer was positioned almost, but not quite, along the anti-diagonal (A) direction, forming a final electric field

$$E_f = \cos\alpha\cos\beta e^{i\phi} \exp(\frac{-(x+\frac{a}{2})^2}{4\sigma^2})|H\rangle + \sin\alpha\sin\beta \exp(\frac{-(x-\frac{a}{2})^2}{4\sigma^2})|V\rangle \tag{2.12}$$

where $\beta = \alpha + \frac{\pi}{2} + \epsilon$ and $\epsilon << 1$. This represents the postselection, where the initial state was projected onto a nearly orthogonal interferometer output. A photodiode placed after the slit measured the intensity distribution, which is equal to the absolute square of E_f:

$$\begin{aligned} I(x) = &\cos^2\alpha\cos^2\beta \exp(\frac{-(x+\frac{a}{2})^2}{2\sigma^2}) + \sin^2\alpha\sin^2\beta \exp(\frac{-(x-\frac{a}{2})^2}{2\sigma^2}) \\ &+ \cos\phi\cos\alpha\cos\beta\sin\alpha\sin\beta \exp(\frac{-(x+\frac{a}{2})^2-(x-\frac{2}{2})^2}{4\sigma^2}) \end{aligned} \tag{2.13}$$

From this, the physics behind the WV is clear. Notice that $I(x)$ is a sum of 3 Gaussians resulting from the complex summation of 2 electric field distributions, as illustrated in Fig 2.3 (with the same parameters used in the Ritchie paper). When $\alpha = \frac{\pi}{4}$ and $\beta = \alpha + \frac{\pi}{2} + \epsilon$, as stated above, the third Gaussian interferes destructively with the first two to create a single Gaussian that is shifted to one side. If ϵ is small but a is not, the distribution shows classic interference fringes. If ϵ is not small, then the final and initial states overlap significantly and the 3 peaks constructively interfere, resulting in one Gaussian that is unshifted.

The center of the shifted distribution can be determined either by directly examining Eqn. (2.13), or from Eqn. (2.5). In this case,

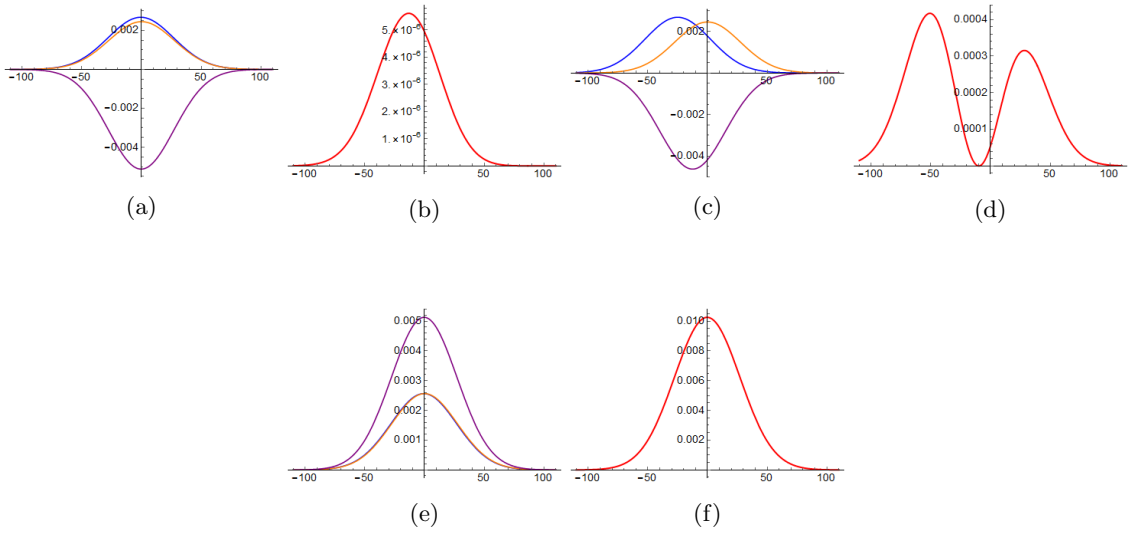

Figure 2.3: The 3 terms in the intensity distribution and the sum of the 3 using parameters from the Ritchie paper ($\sigma = 55\mu m, \phi = 0, \alpha = \frac{\pi}{4}, \beta = \alpha + \frac{\pi}{2} + \epsilon$), for various values of ϵ and a. For (a)&(b) $a = 0.64\mu$m, $\epsilon = 0.022$, for (c)&(d) $a = 25\mu$m, $\epsilon = 0.022$, and for (e)&(f) $a = 0.64\mu$m, $\epsilon = -\frac{\pi}{2}$. The x-axis is position in micrometers and the y-axis is the intensity normalized to the input.

$$
\begin{aligned}
A &= \frac{a}{2}(|H\rangle\langle H| - |V\rangle\langle V|) \\
|\phi_i\rangle &= \cos(\alpha)|H\rangle + \sin(\alpha)|V\rangle \\
|\phi_f\rangle &= \cos(\beta)|H\rangle + \sin(\beta)|V\rangle,
\end{aligned}
\tag{2.14}
$$

which gives $A_w = \frac{1}{2}a\cot\epsilon$.

2.3 Dixon's Ultrasensitive Beam-Deflection Weak Measurement

Work in this thesis grew from an experiment by Dixon et al. [3], which we will discuss now. They demonstrated a WM system to determine the tilt of a mirror with high precision. (The conventional method for measuring a beam tilt is shown in Fig. 2.4(a); one simply looks in the 'far-field' by examining the intensity distribution in at the focal plane of a lens. where the centroid will be shifted by θf.) Their WM setup is shown in Fig 2.4. The system was prepared in a preselected state by splitting a Gaussian beam with a 50/50 beamsplitter (BS), which separates the incoming state into clockwise (CW) and counter-clockwise (CCW) paths.

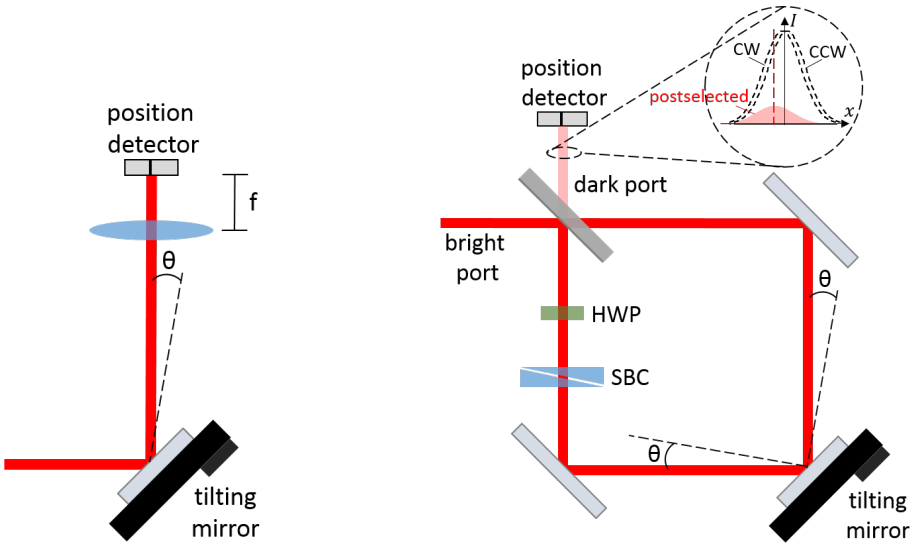

(a) (b)

Figure 2.4: (a) A conventional measurement of a beam deflected at an angle θ. A lens of focal length f focuses the beam onto a position detector positioned a length f away from the lens. A weak measurement of a beam deflection. A 50/50 BS separates light into CW and CCW paths. A small, controllable phase is added with a combination of HWP and SBC such that a small amount of light exits the dark port. The average position of light in the dark port is measured.

$$E_{in} = \frac{1}{\sqrt{2}}[i|\circlearrowleft\rangle + |\circlearrowright\rangle]|H\rangle \exp(\frac{-x^2}{4\sigma^2}) \tag{2.15}$$

A controllable, relative phase is added by a combination of a half-wave plate (HWP) and Soleil-Babinet compensator (SBC). This works because the HWP switches the polarization of the CW path *after* passing through the SBC, but switches the CCW path *before*. The SBC, which is composed of 2 birefringent prisms, is oriented so that its axes align with H and V polarizations. Sliding the prisms relative to each other changes the optical path length of each path separately, so that the desired phase shift can be chosen. When the mirror tilts, a position-dependent phase is created across the beam that is equal and opposite for the two interferometer paths. The resulting state is

$$E_{tilt} = \frac{1}{\sqrt{2}}[ie^{i\frac{\phi}{2}}e^{ikx}|\circlearrowleft\rangle + e^{-i\frac{\phi}{2}}e^{-ikx}|\circlearrowright\rangle]|V\rangle \exp(\frac{-x^2}{4\sigma^2}), \tag{2.16}$$

where $k = k_0\theta$, and θ is the tilt of the beam from the mirror tilting.

To measure the WV, Dixon et al. examined the distribution in the 'dark-port' - the direction of interferometer output opposite of the incoming beam, so named because in order for the WV approximations to be valid ϕ must be small, thus only a small fraction of the light exits via this port (in their case, 2%).

Postselecting on dark-port output results in the state

$$E_{dp} = \frac{1}{2}[-e^{i\frac{\phi}{2}}e^{ikx} + e^{-i\frac{\phi}{2}}e^{-ikx}]\exp(\frac{-x^2}{4\sigma^2})|V\rangle$$

$$= -i\sin(\frac{\phi}{2} + kx)\exp(\frac{-x^2}{4\sigma^2})|V\rangle \ . \tag{2.17}$$

If $(\frac{\phi}{2} + kx) << 1$, we can approximate this as (dropping global phases)

$$(\frac{\phi}{2} + kx)\exp(\frac{-x^2}{4\sigma^2})|V\rangle = \frac{\phi}{2}(1 + \frac{2kx}{\phi})\exp(\frac{-x^2}{4\sigma^2})|V\rangle. \tag{2.18}$$

If $kx << \phi$, then this is approximately

$$\frac{\phi}{2}\exp(\frac{2kx}{\phi})\exp(\frac{-x^2}{4\sigma^2})|V\rangle \ \approx \frac{\phi}{2}\exp(\frac{x - \frac{4k\sigma^2}{\phi}}{4\sigma^2})|V\rangle. \tag{2.19}$$

The intensity profile in the dark-port is given by the absolute square of the electric field amplitude, so

$$I_{dp}(x) = \frac{\phi^2}{4}\exp(\frac{x - \frac{4k\sigma^2}{\phi}}{2\sigma^2}), \tag{2.20}$$

which is the initial Gaussian distribution shifted by $\frac{4k\sigma^2}{\phi}$ and reduced in intensity by a factor of $\frac{\phi^2}{4}$.

If the WV were calculated from Eqn. (2.5), we would use

$$\begin{aligned} A &= k(|\circlearrowleft\rangle\langle\circlearrowleft| - |\circlearrowright\rangle\langle\circlearrowright|) \\ |\phi_i\rangle &= ie^{i\frac{\phi}{2}})|\circlearrowleft\rangle + e^{-i\frac{\phi}{2}})|\circlearrowright\rangle \\ |\phi_f\rangle &= i|\circlearrowleft\rangle - |\circlearrowright\rangle \end{aligned} \tag{2.21}$$

which gives $A_w = -ik\cot\frac{\phi}{2} \approx -ik\frac{2}{\phi}$. Notice that the WV is imaginary, causing a shift $iA_w 2\sigma^2$ in the position basis, instead of the momentum basis.

2.4 Some useful things about weak measurements, and some limitations

Given the amplification from a WM, the natural follow-up question is 'does WM offer an increase in precision over typical methods?' It has been shown that the answer is 'it depends' [14, 15]. In this work, we use the

signal-to-noise ratio (SNR) as our metric to quantify the resolution of a measurement. We will limit our discussion to beam-deflection WM, since that is the focus of our work, but our results could be extended to other types of WM.

For some types of technical noise, e.g., electrical noise in detectors, WM outperform typical methods. In such cases the uncertainty in the measurement is independent of the measurement scheme, but the signal is not. The amplification from WM boosts the signal further above the noise than would typically be possible. Let us examine the case of a beam deflection measurement limited by jitter in the transverse location, σ_j, as is commonly the case when a detector has electrical noise. The SNR in the two cases would be

$$SNR_{conv} = \frac{f\theta}{\sigma_j} \tag{2.22}$$

$$SNR_{WM} = \frac{4k_0\theta\sigma^2}{\phi\sigma_j}, \tag{2.23}$$

Comparing these two, we see that the advantage of a WM over a conventional one would be $\frac{4k_0\sigma^2}{\phi f}$. In fact, Viza et al. [14] demonstrated that any noise source that originated outside of the interferometer is suppressed by the WM technique since it is not amplified in the experiment, as the signal is.

Ferrie and Combs [16] argued that WM are actually suboptimal, since only a subset of the particles that entered the interferometer are indeed detected. They showed that there is some information in the un-postselected particles, and therefore concluded that WM can never be superior. Viza et al. [14] later demonstrated that their point was a rather pedantic one, as in several cases of realistic limitations (detector saturation, detector jitter, angular jitter) 99% of the information is in the postselected photons, so there is little to be gained by measuring un-postselected photons, and in fact the technical noise is reduced.

When the uncertainty is limited by the quantum fluctuations in photon number, as in the case of a laser source with all noises dominated by the laser shot noise, WM perform equally to optimized typical measurements. Barnett et al. [17] showed that the SNR for a shot-noise-limited beam-displacement measurement for a beam of width σ is

$$SNR_{SNL} = \sqrt{\frac{2N}{\pi}}\frac{d}{\sigma}, \tag{2.24}$$

where d is the displacement and N is the number of detected photons.

Starling et al. [15] extended Barnett's analysis to show that the optimal conventional setup for determining a beam tilt was to use a lens to focus the beam and measure the position shift at the focal point. At the focal point, the tilt θ would cause a shift $d_f = f\theta$ and the beam width would be $\sigma_f = \frac{f}{2k_0\sigma}$ This would

give the SNR

$$SNR_{conv} = \sqrt{\frac{2N}{\pi}} 2k_0 \sigma\theta. \tag{2.25}$$

In a WM of the beam tilt, the beam size would not change, but the displacement would be $\frac{4k\sigma^2}{\phi}$ (from Eqn. (2.20)), while the number of detected photons is decreased by the postselection probablility, $\frac{\phi^2}{4}$, resulting in the SNR

$$SNR_{WM} = \sqrt{\frac{2N}{\pi}} 2k_0 \sigma\theta. \tag{2.26}$$

This is the same as the conventional measurement, yet with only a small percentage of N actually hitting the detector! We will explore this more in the next chapter.

Chapter 3

Recycled Weak Measurements

3.1 Recycling and Why It's Useful

Given that the same SNR can be achieved with a single weak measurement (in which only a few percent of the input photons are actually detected) compared to a conventional measurement (where all input photons are detected), we investigated whether the unpostselected photons could be taken advantage of. Instead of simply throwing away most of the input light, we sought to demonstrate the benefits of recycling light from the bright port until it is either detected or lost. In this section we will discuss the potential improvements from recycling [1]. The theory presented here was published by Dressel et al. in [20].

From Section 2.4, we saw that

$$SNR \propto \sqrt{N}, \tag{3.1}$$

where N is the number of detected photons. If photons are sent through the system one time (a single-pass WVM),

$$N \propto \eta N_i, \tag{3.2}$$

where $\eta = \frac{\phi^2}{4}$ is the postselection probability and N_i is the number of input photons. For an R-pass WVM,

$$N \propto \sum_{p=1}^{p=R} (1-\eta)^{p-1} \eta N_i = [1-(1-\eta)^R] N_i. \tag{3.3}$$

The improvement in the SNR over a single-pass measurement is then

$$SNR_R SNR_1 = \sqrt{\frac{1-(1-\eta)^R}{\eta}}. \tag{3.4}$$

[1] Our method of *discrete* recycling - sending all the photons back through the system - should not be confused with the continuous power-recycling technique [18], which was recently demonstrated [19]. See Section 3.4 for more discussion.

For small η and small R, this is $\approx \sqrt{R}$, or for infinitely many passes, $\approx \sqrt{\frac{1}{\eta}}$.

Note that the dominant effect from recycling is to increase the number of photons at the detectors, as opposed to increasing the displacement from the tilting mirror (a common misinterpretation). To see why the displacement is not multiplied by passing through the system multiple times, one can examine Eqn. (2.16), but projecting onto the bright port instead of the dark port. This gives the electric field

$$E_{bp} = \frac{i}{2}[e^{i\frac{\phi}{2}}e^{ikx} + e^{-i\frac{\phi}{2}}e^{-ikx}]\exp(\frac{-x^2}{4\sigma^2})$$

$$= i\cos(\frac{\phi}{2} + kx)\exp(\frac{-x^2}{4\sigma^2}). \tag{3.5}$$

If $(\frac{\phi}{2} + kx) << 1$, we can approximate this as (dropping any squared terms and global phases)

$$[1 + \frac{1}{2}(\frac{\phi}{2} + kx)^2]\exp(\frac{-x^2}{4\sigma^2}) \approx [1 + \frac{\phi kx}{2}]\exp(\frac{-x^2}{4\sigma^2}); \tag{3.6}$$

if $\frac{\phi kx}{2} << 1$, then this is approximately

$$\exp(\frac{\phi kx}{2})\exp(\frac{-x^2}{4\sigma^2}) \approx \exp(\frac{-(x + \sigma^2\phi k)^2}{4\sigma^2}). \tag{3.7}$$

This is the same Gaussian we started with, shifted by $\sigma^2\phi k$, which is small compared to σ. Essentially, the bright port beam is the same as the input beam, so the displacement in the darkport should be independent of the number of passes. Therefore, any benefits come from increasing the number of detected photons. Note that after a large number of passes, the effects of small modifications in the bright port mode add up and become non-negligible, as we will discuss next.

3.1.1 Beam Reshaping

As the beam cycles and a subset of photons are postselected, the original distribution is in fact slightly changed each pass. We can calculate the dark-port intensity on any given isolated pass from Eqns. (2.17) and (3.5) (as shown in [20])

$$I_{pi} = (1 - \gamma)^p \cos^{2(p-1)}(\frac{\phi}{2} + kx)\sin^2(\frac{\phi}{2} + kx)\exp(\frac{-x^2}{2\sigma^2}), \tag{3.8}$$

where p is the pass number and γ is the per-pass loss. To find the cumulative intensity distribution after p passes, we can sum over Eqn. (3.8):

$$I_{pc} = \sum_{r=1}^{p} I_{ri} = (1-\gamma)\frac{1-[(1-\gamma)\cos^2(\frac{\phi}{2}+kx)]^p}{1+\gamma\cot^2(\frac{\phi}{2}+kx)}\exp(\frac{-x^2}{2\sigma^2}). \tag{3.9}$$

Notice that if $\gamma = 0$ (no loss) and $p = \infty$ (pulses were trapped until detected), in Eqn. (3.9) the original, unshifted Gaussian is recovered! In other words, the displacement would be zero and the signal completely lost. In extreme cases, additional measures would need to be taken to prevent the signal from vanishing.

With our real-world losses, the decrease in the signal is much less dramatic. Fig. 3.1 shows the expected cumulative signal over our 27 passes. We see the signal from the first pass, $\langle x_1 \rangle$, degrades to $\langle x_{27} \rangle = 0.87\langle x_1 \rangle$. This is sufficient to see a significant improvement in SNR over a single pass, so we have chosen not to correct for this effect. This could be accomplished, e.g. if the postselected distribution were pulled from *opposite* sides with each pass, which could be done by designing an odd number of reflections into the system such that the profile is flipped on consecutive passes.

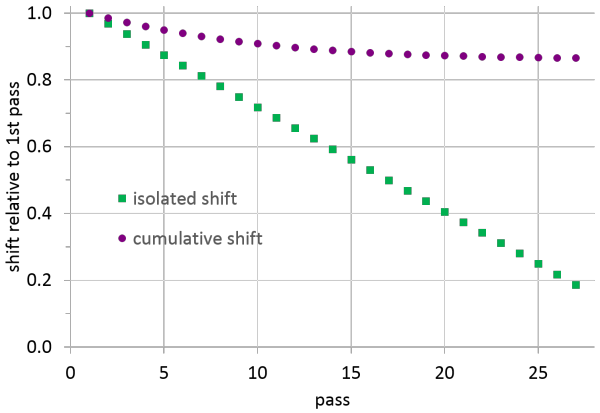

Figure 3.1: The effects of reshaping on the shift of the isolated (green squares) and cumulative (purple circles) distributions as a function of pass number using measured parameters ($\sigma = 86\mu$m, $\gamma = 19\%$, and $\phi = 0.35$ (which gives 3% postselection probability)).

3.2 Designing a Weak Measurement Recycling System

Our complete design for a recycled weak measurement of a beam deflection is shown in Fig. 3.2. Because our setup requires many pieces working together, we will give a brief overview here and then discuss the more intricate parts in greater detail in the following 4 subsections for clarity.

Our weak measurement interferometer is similar to that of Dixon et al. [3]. In the bright port we added a recycling loop with a polarization switch (see Section 3.2.1) that traps the pulses for up to 27 passes. A position detector (see Section 3.2.3) designed for low-photon-number detection measures the displacement from tilting a mirror in a piezo-controlled mount (Thorlabs KC1-PZ).

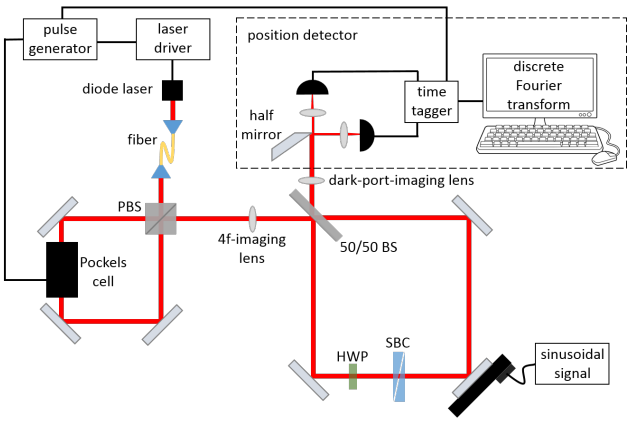

Figure 3.2: Our setup for recycling bright port photons in a weak measurement of a beam tilt. A pulse generator (with controllable delays) triggers the laser, PC, and timetagger. H-polarized laser pulses enter the system, are passed through an unactivated PC, and are transmitted to the WM interferometer. The combination of HWP and SBC controls the relative phase between the CW and CCW paths while also flipping the polarization to V. In the interferometer, photons are incident on a piezo-driven mirror tilted at a frequency of 500 Hz. Approximately 3% of incoming photons exit the dark port and are detected, while 97% are recycled in the bright port. Recycled photons are reflected at the PBS and switched back to H polarization by the now-activated PC. Photons that exit through the dark port are split into left and right halves of the beam, where 2 APD's measure the difference in counts. Counts are registered by a timetagger and later analyzed in MATLAB to obtain the amplitude of the oscillation of the counts difference.

Our light source is a 690-nm diode laser (Opnext HL6738MG) pulsed at 200 kHz with approximately 600-ps pulsewidth. We attenuate the laser such that only one photon at a time is likely to be detected (i.e., our count rate on each detector is 20 kHz or less). The laser output is coupled through a single-mode fiber with a microscope objective (Newport M-40X) and adjustable beam-expander (Special Optics Model 56-30-2-8X) at the fiber output, which allows us to control the beam waist and position. A horizontal (H) polarizer is also placed at the fiber output. A 4f-imaging system (see Section 3.2.2) prevents the beam from expanding as it traverses through the 1.3-meter loop 27 times.

The number of round trips in the recycling system is limited by the postselection probability and the loss from scattering on optical components. We chose a postselection probability of 3%, corresponding to a relative phase between the CW and CCW paths of $\phi = 0.35$. This places us well within the approximations we made in finding the weak value, namely $k_0\theta\sigma < \phi < 1$. (In our case, $\sigma = 86$ μm and the maximum tilt on the mirror is $\theta = 7.5$ μrad, so $k_0\theta\sigma = 5.9$ mrad.) Loss from our optics is approximately 16%, resulting in a total per-pass loss of about 19%. The total loss was determined by fitting the transmission versus pass number, $T(p) = e^{-\gamma p}$, then deducing the average per-cycle loss from $L_{avg} = 1 - T_{avg} = 1 - e^{-\gamma}$. The cutoff for including passes in our measurement was somewhat arbitrary; we chose not to include passes that had less than about 0.5% of the number of counts in the first pass. A representative plot of counts is shown in

Fig. 3.3.

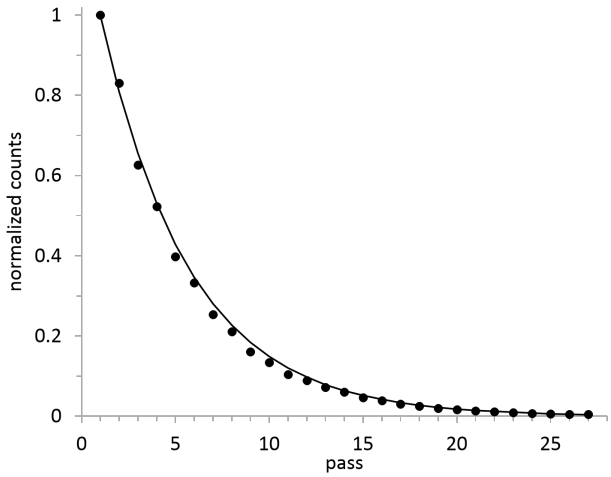

Figure 3.3: A representative plot of counts vs. pass number. The black circles are data, the line is an exponential fit, which shows an average per-pass loss of 19%, including 3% from postselection.

Data is collected with 2 avalanche photodiodes (APD's) (Perkin Elmer SPCM-AQR-13 and SPCM-AQR-14), a timetagger (quTools, quTau model), and MATLAB software. A fast-Fourier transform is used to determine the average shift from the tilting mirror.

3.2.1 A Polarization Switch

As we discussed in Section 2.3, each traversal through the weak measurement interferometer switches the polarization from H to V. Thus, light transmitted by the PBS before entering the interferometer is reflected after exiting it. Since the first pulse is H polarized by design, it needs to pass through the recycling loop without being changed. On every subsequent pass the polarization needs to be flipped from V to H. This is accomplished with the use of a Pockels cell (PC) and fast driver (BME Bergmann PCD7a). A PC is a crystal (in this case, RTP from Raicol Crystals) with birefringence that depends linearly on the strength of an electric field applied in one direction. Therefore, by controlling the applied field strength we can choose the relative phase between the ordinary and extraordinary axes and make a waveplate that can be switched off and on. The driver is triggered by a SRS DG535 pulse and delay generator, which also triggers the laser driver so that the two are synchronized. The PC driver has a rise time of 2.2 ns, during which the PC voltage switches from 0 to 875 V. The PC is aligned so that at 0 V the polarization is unaffected, but at 875 V it is rotated by 90^o. The voltage switches from low to high voltage between the first and second passes, and remains high for $\sim$420 ns after the first, so each pulse is switched from V to H polarization.

3.2.2 Preventing the Beam from Expanding

Photons are trapped in our recycling system for ∼27 passes before they are detected (∼20%) or lost (∼80%). Each round trip is about 1.3 meters, which means some photons travel up to 35 meters. As our beam would expand and become too huge without optics to prevent it, we designed a 4f-imaging system such that the beam is identical on every pass. A lens of focal length f = 300 m is placed in the middle of the loop, such that there is a distance f from the lens to the mid-point of both the recycling loop and the interferometer. Because the distance from the tilting mirror (where the beam waist is located) to the position detector is longer than the Rayleigh range of the beam, without any extra optics the beam expands from about 86 μm to about 220 μm. This causes the SNR in the measurement to decrease. To correct for this effect, we added a lens in the dark port to image the waist onto the position detector (described below), which recovers the best possible SNR. The full imaging system is described in more detail in Appendix A.

3.2.3 Position Detector

The displacement in the dark port due to the mirror tilting is determined by our position-detector which was designed to work at the few-photon level. A D-shaped mirror (Thorlabs BBD1-E02) reflects the right half of the beam to one APD while the left half of the beam is incident on the other APD. Pulses are fed into a timetagger, which records the arrival time with 81-ps precision. Timing data is uploaded into MATLAB for analysis.

3.2.4 Data Collection

The observed displacements in our experiment are on the order of 1 μm, which is much smaller than the drift we observe in the beam position. To overcome the large amount of DC noise, we instead drive the mirror to tilt at a frequency of 500 Hz and observe the magnitude of the position oscillation at that frequency. In this regime, the position uncertainty is dominated by the laser shot noise. We see approximately 3×10^3 counts per second in the first pass on each detector, and about 20×10^3 counts per second on each detector in all passes. Time tags are divided into 100-μs bins (corresponding to 20 laser pulses or an average of ∼2 photons per bin). Finally, a discrete Fourier transform with data taken over approximately 300 s is computed using MATLAB. The relevant timescales involved in this experiment are show in in Fig 3.4. The process is described in more detail in Appendix B.

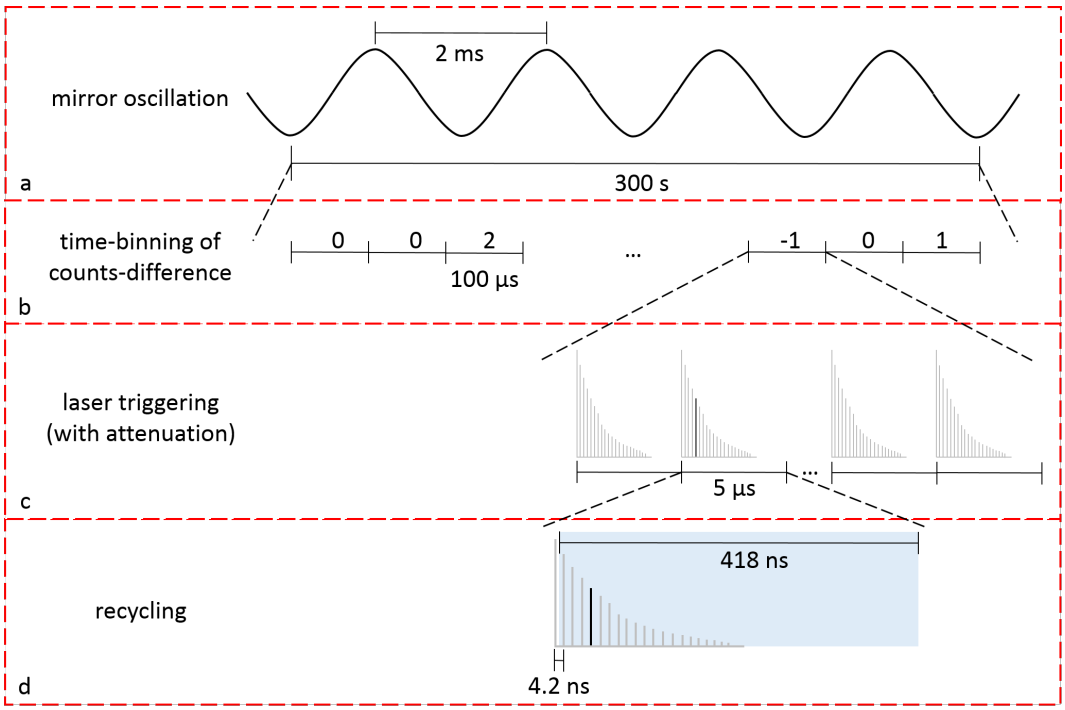

Figure 3.4: The relevant timescales in our pulse-reyclcing setup. Box (a) shows the oscillation of the mirror angle, which causes an oscillation in the beam position in the dark port and, correspondingly, an oscillation in the counts difference between the 2 APD's. Box (b) shows how the counts difference is divided into 100-μs bins for FFT analysis. Box (c) demonstrates how the laser fires a pulse every 5 μs, with a 10% chance of any given pulse containing a photon (here represented by the black line). Box (d) shows a loop-time of 4.2 ns, caused by the PC switching on after the first pass and remaining on until the photon is detected or lost.

From the discrete Fourier transform, we obtain amplitude information over a spectrum of frequencies. The signal is the average amplitude at 500 Hz, and the noise is the root-mean-square of the surrounding off-signal frequencies.

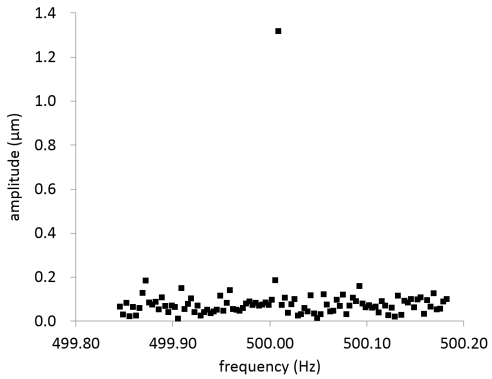

Figure 3.5: A representative sample of the FFT output. The signal is at a single frequency near 500 Hz, while surrounding frequencies show the amplitude noise. The uncertainty in the signal amplitude is calculated from the RMS of the surrounding frequencies.

3.3 Results and Discussion

We first confirmed that our experiment was indeed shot-noise limited by confirming that the uncertainty in our position measurement scales as $\frac{1}{\sqrt{N}}$. Results are shown in Fig. 3.6.

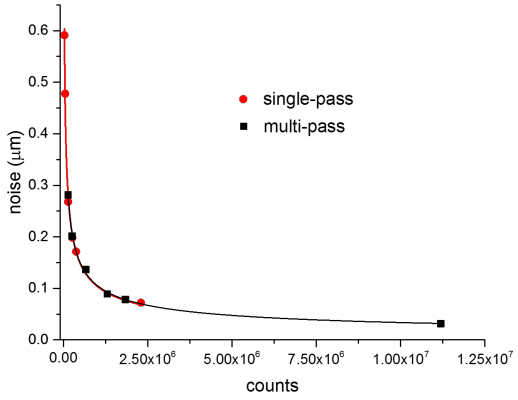

Figure 3.6: The measured noise vs total detected counts for a single-pass WM (red circles) and a recycled WM (black squares). Solid lines are fit to the equation ax^b, where we expect $b = -0.5$, i.e., the noise should scale as $\sqrt{N}$. The fit gives $b = -0.51 \pm 0.02$ for the single WM, and $b = -0.50 \pm 0.01$ for a recycled WM.

Next, we looked at the signal increase from recycling. Fig. 3.7 shows the observed signal for multi-pass and single-pass WM. To obtain the average signal for each mirror tilt, we averaged 10 measurements of the FFT amplitude at 500 Hz. To obtain the error bars, we averaged the RMS from 100 surrounding frequencies (from about 499.85 to 500.18 Hz, with 3.3 mHz spacing) from 2 trials. The average increase in counts with recycling was 5 times that without recycling, so we expect our recycling signal to be 4.35 times the signal without recycling when reshaping effects are accounted for. When we plotted signal versus mirror tilt, we saw a slope of 4.0 ± 0.1 μrad^{-1} for multi-pass measurements, while for the single-pass measurements we saw a slope of 0.91 ± 0.04 μrad^{-1} (only including points with a SNR above 1). This represents a signal increase by a factor of 4.4 ± 0.2, in good agreement with our expectations.

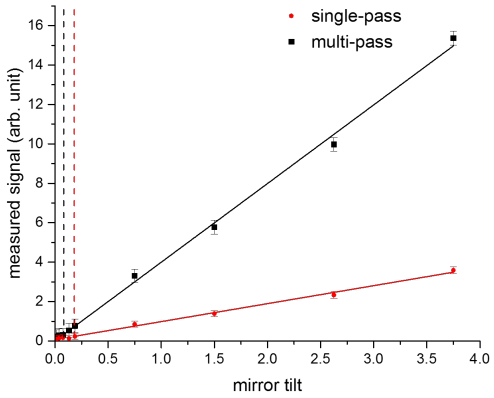

Figure 3.7: The measured signal versus mirror tilt from recycling (black squares) and without recycling (red circles). The black line is a linear fit with a slope of 23 ± 1, the red line has a slope of 4.6 ± 0.2. The dotted vertical lines show where we expect the SNR ratio to be 1.

To compare the resolution achievable with each method, we then measured the SNR as a function of the input photon number for a multi-pass WM, a single pass WM, and a conventional measurement, as shown in Fig. 3.8a. For each point, we averaged 20 measurements of the FFT amplitude at 500 Hz. To obtain the error bars, we averaged the RMS from 100 surrounding frequencies from 4 trials. Note that the SNR for a single WM and a conventional measurement are nearly the same, as we expected from Eqns. (2.25) and (2.26). The average increase of the multi-pass SNR over the single-pass SNR is a factor of 2.10 ± 0.06, as determined from Fig. 3.8b, in good agreement with our expectation of 1.95 (including reshaping effects).

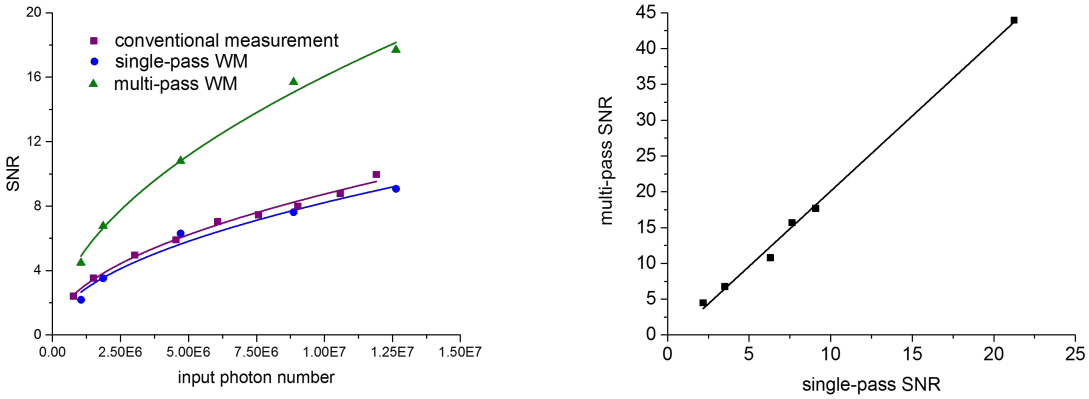

(a) (b)

Figure 3.8: (a) The measured SNR vs input photon number for a conventional measurement, a single-pass WM, and a multi-pass WM. Solid lines are fit to the equation ax^b, where we expect $b = 0.5$. The fit gives $b = 0.49 \pm 0.02$ for the conventional measurement, $b = 0.53 \pm 0.03$ for the recycled WM, and $b = 0.50 \pm 0.05$ for the single WM (b) A linear fit of the SNR with recycled WM vs. no recycling. The slope is 2.10 ± 0.06, indicating the improvement in resolution with recycling.

3.4 A Note on Power Recycling

Pulse recycling is only one method of implementing recycling. Lyons et al. [18] suggested a related but different technique based on 'power recycling'; instead of using a discrete number of cycles (with short optical pulses to define them), the entire system is operated with narrow bandwidth continuous-wave light. Light in the bright port is constantly recycled by effectively converting the WM interferometer into one mirror of a resonant cavity. This has been demonstrated experimentally by Wang et al. [19]. Instead of using a PBS and PC, they placed a curved mirror in the bright port which formed a resonant cavity with the WM interferometer. This increased the count number on their detectors and increased the SNR in their experiment. Though they reported a signal increase of only 2.4 (which should correspond to a resolution increase of 1.5), we think this method probably holds more potential to be useful, as the setup can be more compact and there is no need for a fast, high-voltage polarization switch. They were mainly limited by the losses in their optics, which coupled with the postselection probability gave them a 40% per-pass loss. This could probably be significantly improved.

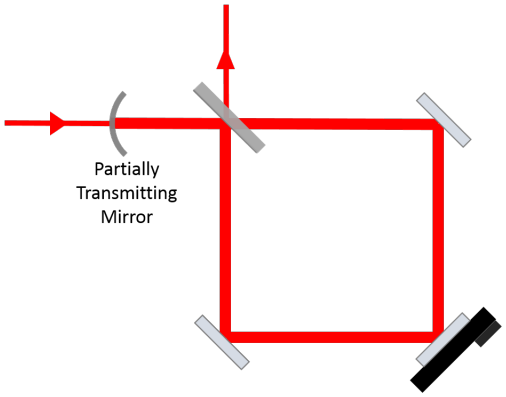

Figure 3.9: A rough sketch of the setup for power recycling as demonstrated by Wang et al. [19], using a mirror to form a resonant cavity with the WM interferometer.

Chapter 4

Spatial Entanglement

4.1 Spontaneous Parametric Down Conversion

Spontaneous parametric downconversion (SPDC) has been known for some time to produce tight correlations in photon properties, and it has been utilized in numerous experiments. In this work, we aim to demonstrate an improvement in the precision of determining a beam position by utilizing the nonclassical position correlations between two downconverted photons.

SPDC is the process by which a high-energy pump photon is converted into two daughter photons. It is called 'spontaneous' because the process occurs with no external control field (i.e. it is stimulated by vacuum fluctuations), 'parametric' because the total light energy is the same before and after the process, and 'downconversion' because energy conservation implies that the daughter photons are of lower energy than the parent pump photon. SPDC occurs through a non-linear interaction between the electric field of light and the polarization of atoms in a crystal. For crystals without inversion symmetry (i.e. crystal that display a second-order response to an input field), the polarization can be written as

$$\overrightarrow{\mathbf{P}} = \chi^{(1)}\overrightarrow{\mathbf{E}} + \chi^{(2)}\overrightarrow{\mathbf{E}}^2, \tag{4.1}$$

where $\chi^{(1)}$ and $\chi^{(2)}$ are the first- and second-order optical susceptibilities and $\overrightarrow{\mathbf{P}}^{(2)} \equiv \chi^{(2)}\overrightarrow{\mathbf{E}}^2 = \chi^{(2)}_{ijk}E_iE_j$ in Einstein notation. If the input field is a sum of waves at two frequencies

$$\overrightarrow{\mathbf{E}} = \overrightarrow{\mathbf{E}}(\omega_1) + \overrightarrow{\mathbf{E}}(\omega_2) = \overrightarrow{\mathbf{E}}_1(e^{i\omega_1 t} + e^{-i\omega_1 t}) + \overrightarrow{\mathbf{E}}_2(e^{i\omega_2 t} + e^{-i\omega_2 t}) \tag{4.2}$$

then $P^{(2)}_k$ will have eight terms in it, two of which are $e^{i(\omega_1+\omega_2)t}$ and $e^{-i(\omega_1+\omega_2)t}$. These correspond to sum-frequency generation, in which two input waves mix via the nonlinear material to form a third, higher-frequency wave. SPDC is in fact the inverse of sum-frequency generation, but unlike sum-frequency generation it has no classical explanation, as the pump photon is stimulated to decay into the two daughter photons by vacuum fluctuations. The probability that any given pump photon will downconvert is low, typically

10^{-9}, due to the small value of $\chi^{(2)}$ in most materials. For more about nonlinear optical effects, see [21].

Because downconversion is an energy-conserving process, we know

$$\omega_p = \omega_1 + \omega_2 \tag{4.3}$$

where ω_p, ω_1, and ω_2 are the frequencies of the pump and daughters, respectively. In order for SPDC to occur at all, though, momentum must also be conserved

$$\vec{\mathbf{k}}_p = \vec{\mathbf{k}}_1 + \vec{\mathbf{k}}_2 \tag{4.4}$$

where $\vec{\mathbf{k}}_p$, $\vec{\mathbf{k}}_1$, and $\vec{\mathbf{k}}_2$ are the wavevectors of the pump and daughters, respectively, and $|\vec{\mathbf{k}}| = \frac{2\pi n(\lambda)}{\lambda} = \omega c n(\omega)$. This condition is called phase-matching. It is the trickier part of producing downconverted photons, since crystals generally have a wavelength-dependent refractive index, and that makes matching the speed of the pump and daughters, which typically have wavelengths hundreds of nanometers apart, a non-trivial task. One solution is to use a material with a refractive index that depends on the polarization, called a birefringent material. In uniaxial birefringent crystals (meaning that there is one axis in the crystal with refractive index different than the other two axes), phase matching can be achieved by tilting the axis of the unique plane (called the optic axis) relative to the pump direction, as illustrated in Fig. 4.1. There are multiple ways to use birefringence to achieve phase-matching; in type-I phase-matching the downconverted photons have the same polarization, while in type-II they have opposite polarizations. For more details on phase-matching see [21], or [22] for an example of calculating the crystal angle for type-I phase-matching.

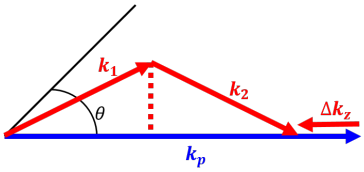

Figure 4.1: Phase-matching in downconversion inside a crystal. θ is the angle between the pump wavevector and optic axis, and determines the momentum of the pump in the crystal. The wavevectors of the downconverted photons must match the pump such that Δk_z is small, or the process will not occur.

In this work, we chose to use Type-II SPDC, to easily separate the photons by their polarization. We also chose a crystal angle such that the downconversion photons were collinear, meaning they were both in the same spatial mode as the pump. Because the downconverted photons in Type-II phase-matching have orthogonal polarizations and experience different refractive indices, they must be emitted from the pump into two separate cones. Type-II collinear SPDC is accomplished by selecting the crystal angle such that the cones are tangent to each other and intersect along one line parallel to the pump, then selecting only

photons detected in that direction.

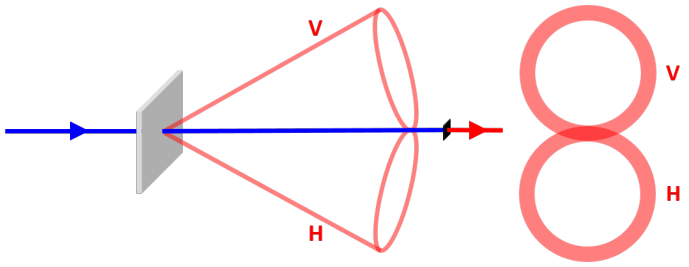

(a) (b)

Figure 4.2: (a) shows a schematic of Type-II collinear SPDC. The daughter photons are born into two tangent cones. The biphoton is collinear with the pump in the region where the cones overlap. The pump is filtered to achieve two daughter photons in the same mode. (b) shows the process as viewed looking straight into the pump.

4.2 The Spatial Profile of Type-II Collinear SPDC

Schneeloch and Howell [23] wrote a detailed tutorial for determining the spatial probability distribution of collinear SPDC; here we will discuss the highlights. They showed that the joint-probability amplitude of the two downconverted photons could be written as;

$$\Phi(\overrightarrow{\mathbf{k_1}}, \overrightarrow{\mathbf{k_2}}) = \mathcal{N}\,\mathrm{sinc}(\frac{\Delta k_z L_z}{2}) e^{-\sigma_p^2 |\overrightarrow{\mathbf{q_1}} + \overrightarrow{\mathbf{q_2}}|^2}, \tag{4.5}$$

where $\overrightarrow{\mathbf{k_1}}$, $\overrightarrow{\mathbf{k_2}}$ are the wavevectors of the two photons, $\Delta k_z \equiv k_{pz} - k_{1z} - k_{2z}$ as in Fig. 4.1, and $\overrightarrow{\mathbf{q_1}}$, $\overrightarrow{\mathbf{q_2}}$ are their wavevectors in the transverse direction. We can understand this equation by breaking it into pieces; the Gaussian factor is identical to the amplitude of the pump in the transverse direction, since momentum must be conserved. The sinc factor will only contribute significantly if Δk_z is small for the same reason, so we refer to it as the phase-matching factor [1].

We are interested in the position-space joint amplitude of the biphotons in the xy plane, as that is where we will measure our beam displacement. Toward that end, Eqn. (4.5) can be rewritten in terms of the transverse momenta by using momentum conservation (see Fig. 4.1);

[1] To understand why the momentum amplitude appears as a sinc function in Δk_z, we note that the evolution of the pump state in the crystal is calculated via time-dependent perturbation theory, which says $|\Psi(t)\rangle = (1 - \frac{i}{\hbar}\int_0^t H(t')dt')|\Psi(0)\rangle$. The Hamiltonian for electric fields is $\frac{1}{2}\int \overrightarrow{\mathbf{D}} \cdot \overrightarrow{\mathbf{E}} d^3r$, where $\overrightarrow{\mathbf{D}} = \epsilon_0 \overrightarrow{\mathbf{E}} + \overrightarrow{\mathbf{P}}$. $\overrightarrow{\mathbf{P}}$ depends on $\overrightarrow{\mathbf{E}}^2$ inside the crystal as we saw in Eqn. (4.1), so the state of the downconversion will depend on $\int \overrightarrow{\mathbf{E}}^3 d^3r$, which when quantized represents the product of the field operators of the pump and daughter photons. Since $E_z \propto e^{ik_z z}$ and $\int_{-\frac{L_z}{2}}^{\frac{L_z}{2}} e^{ik_z z} dz = \mathrm{sinc}(\frac{k_z L_z}{2})$, we have our phase-matching factor as in (4.5). In short, the sinc function appears because the fields interact with each other over a region with sharp boundaries, i.e. the crystal.

$$k_p = (k_1 + k_2)\cos(\theta) - \Delta k_z \tag{4.6}$$

$$k_1 \sin(\theta) = \frac{|\overrightarrow{\mathbf{q_1}} - \overrightarrow{\mathbf{q_2}}|}{2} \tag{4.7}$$

By using the small-angle approximation, solving for θ in Eqn. (4.7), plugging into Eqn. (4.6), and solving for Δk_z, we find

$$\Delta k_z \approx \frac{|\overrightarrow{\mathbf{q_1}} - \overrightarrow{\mathbf{q_2}}|^2}{2k_p}. \tag{4.8}$$

Inserting Eqn. (4.8) into Eqn. (4.5) gives

$$\Phi(\overrightarrow{\mathbf{k_1}}, \overrightarrow{\mathbf{k_2}}) = \mathcal{N}\,\mathrm{sinc}(\frac{L_z \lambda_p}{8\pi}|\overrightarrow{\mathbf{q_1}} - \overrightarrow{\mathbf{q_2}}|^2) e^{-\sigma_p^2 |\overrightarrow{\mathbf{q_1}} + \overrightarrow{\mathbf{q_2}}|^2}. \tag{4.9}$$

It is convenient to define

$$k_+ \equiv \frac{k_{1x} + k_{2x}}{\sqrt{2}} \tag{4.10}$$

$$k_- \equiv \frac{k_{1x} - k_{2x}}{\sqrt{2}} \tag{4.11}$$

so that we can work in one dimension (since it is the same in both dimensions anyhow). Then Eqn. (4.9) reads:

$$\Phi(k_+, k_-) = \mathcal{N}\,\mathrm{sinc}(\frac{L_z \lambda_p}{4\pi} k_-^2) e^{-2\sigma_p^2 k_+^2}. \tag{4.12}$$

From here, we can transform into position-space. This is almost an easy task, as we have two separable terms depending on k_+ and k_-, one of which is a Guassian. Transforming $\mathrm{sinc}(k_-^2)$, however, is not so simple. Schneeloch and Howell circumvented this issue by approximating Eqn. 4.12 as a double-Guassian. The joint probability distribution of the biphotons would then look like:

$$P(x_1, x_2) = \exp(-\frac{(x_-)^2}{2\sigma_-^2}) \exp(-\frac{(x_+)^2}{2\sigma_+^2}) \tag{4.13}$$

where

$$x_+ = \frac{x_1 + x_2}{\sqrt{2}} \tag{4.14}$$

$$x_- = \frac{x_1 - x_2}{\sqrt{2}} \tag{4.15}$$

and $\sigma_+^2 = 2\sigma_p^2$. It is less straightforward to define σ_-, because the distribution is not actually Gaussian. Schneeloch and Howell pointed out that there are several ways to do it, depending on the purpose. They found that the distribution most closely resembled the exact transform of Eqn. 4.12 across the central peak if they set Eqn. 4.13 equal to the exact transform of Eqn. 4.12 at $x_+ = x_- = 0$ and solved for σ_-. In that case, they approximated

$$\sigma_- = \sqrt{\frac{4L_z\lambda_p}{18\pi}}. \tag{4.16}$$

The position joint probability distribution is shown in Fig. 4.3. We see that the distribution can be written as two independent terms representing the profile along x_+ (with width σ_+), and along x_- (with width σ_-). The spread along x_+ is determined by the pump width, since this term tells us about the average position of the pairs, which can be born anywhere the pump exists. The spread along x_- is determined by the momentum correlations, which we saw will be determined by the length of the crystal, L_z. This has an intuitive explanation; longer crystals result in a tighter momentum correlation from phase matching, causing weaker transverse spatial correlations.

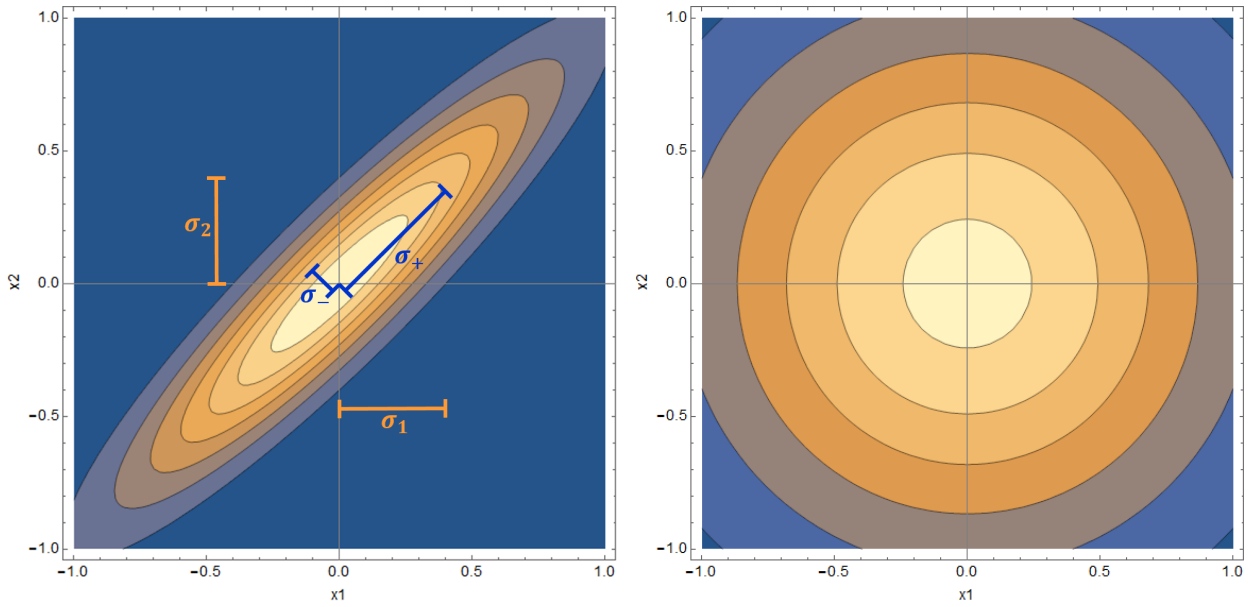

(a) (b)

Figure 4.3: The joint probability distribution of type II collinear SPDC when (a) $\sigma_+ = 5\sigma_-$ and (b) when $\sigma_+ = \sigma_-$

From Eqn. (2.24) we know that the uncertainty in a beam displacement measurement is directly proportional to the width of the beam. Therefore, one may strongly suspect upon inspecting Fig. 4.3 that the position correlations in the SPDC potentially offer an increased resolution over the pump beam, if the

photons are displaced in a way that shifts the distribution along x_-. Lyons et al. showed in [24] that such intuition is indeed correct, and the noise reduction is

$$\frac{\sigma_e}{\sigma_{ue}} = \frac{\sigma_-}{\sigma_+}, \tag{4.17}$$

where σ_e is the uncertainty in the entangled case, as in Fig. 4.3(a), and σ_{ue} is the uncertainty for the unentangled case, as in Fig. 4.3(b).

Interestingly, the size of the beam that interacts with the environment is equal to the projection onto the x_1 or x_2 axis, as this is the width of each of the biphotons. Thus it is possible to achieve a measurement with resolution σ_- with a beam approximately the size of σ_1.

Chapter 5

Entanglement-Enhanced Precision Spatial Measurements

5.1 Displacement Measurements With a 2D Distribution

In this chapter, we will explore the use of spatial entanglement to significantly improve the achievable resolution of a displacement measurement over that with classically uncorrelated light.

We saw in Fig. 4.3 that the spatial correlations inherent to SPDC from the phase-matching conditions offer an increased resolution for displacements in the x_- direction. Since x_- is a rotated coordinate depending on x_1 and x_2, which are the positions of each of the daughter photons and correspond to easily accessible variables in the lab, let us first discuss how to set up this experiment such that we get a displacement in the x_- direction.

A positive shift in $x_- \equiv \frac{x_1 - x_2}{\sqrt{2}}$ corresponds to x_1 getting larger while x_2 gets smaller. We had two options to achieve this: either design a system that gives opposite displacements to the two photons, or flip the basis of one of them and give them the same displacement. The first is not desirable, as it would be cumbersome to implement and essentially useless for any real-world applications. The second adds a bit of complexity to the setup, but is easily achievable by simply giving one photon an odd number of reflections and the other an even number before they are displaced.

It is not immediately clear how one would set up detectors to capture the correlations. We saw in Chapter 3 that for independent photons, scaling the difference in counts between the left and right halves of the beam gives an accurate measure of the displacement. One may naively try to divide the distribution in Fig. 4.3 along the diagonal, but that would require a large number of pixels, a difficult feat with conventional APDs. Instead, Lyons et al. showed in [24] that the two-photon equivalent of a split detector can be made by splitting each of the photons into left and right halves and estimating the deflection with the following formula:

$$d = \frac{\sqrt{\pi(\sigma_-^2 + \sigma_+^2)}}{2} \frac{C_{RR} - C_{LL}}{C_{RR} + C_{LL} + C_{LR} + C_{RL}}, \tag{5.1}$$

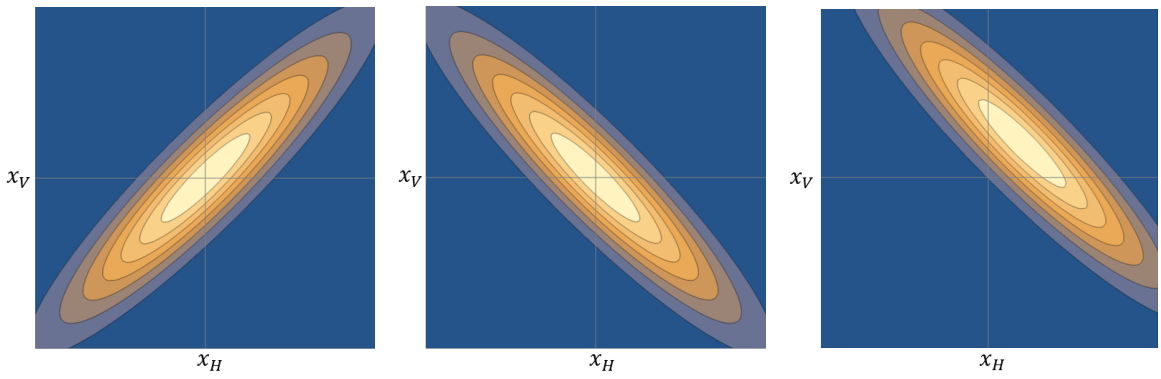

(a) (b) (c)

Figure 5.1: (a) The theoretical position joint-probability distribution of the biphoton in the plane of the crystal, where it shows strong positive correlations. (b) The spatial distribution after the H photon is reflected twice while the V photon is reflected three times. The extra reflection flips the distribution about the x-axis. (c) The distribution after being displaced by the moving mirror; note that it shifts along the narrow axis of the final joint spatial distribution.

where C_{RR} and C_{LL} are the number of coincidences involving photons that both land on the right or left, respectively, and C_{RL} and C_{LR} are coincidences landing on opposite sides. The idea is illustrated in Fig. 5.1. With this in mind, we will discuss our implementation of a deflection measurement using SPDC.

5.2 The Experimental Setup

Our setup is shown in Fig. 5.2. A 355-nm laser (Coherent, model Paladin Compact 355-4000) polarized along V pumps a BBO crystal (from Newlight, cut to 48.6^o to enable Type-II phase matching) with optic axis also aligned along V. The pump is removed with a low-pass spectral filter and the SPDC wavelength is selected with a second, narrow filter centered at 711 nm with a 25-nm bandwidth (Semrock FF01-711/25-25).A 175-mm lens (Edmund Optics 49-363) placed 175 mm from the crystal collimates the collected downconversion photons. A PBS then splits the biphoton by polarization; we will label them by their polarizations at the PBS for simplicity. The H photon passes through a QWP positioned at 45^o and is reflected at normal incidence by a mirror, so that upon return to the PBS it is now V polarized and reflected to the displacing mirror. The V-polarized downconversion photon is reflected by the PBS and two mirrors positioned at 45^o toward the displacing mirror. Note that the x-coordinate of the V photon is flipped relative to the H photon, converting positive spatial correlations in the crystal to negative correlations on the displacing mirror; this allows a lateral displacement of both beams to shift the joint-probability distribution along the narrow direction. For convenience, the displacing mirror actually consists of two separate mirrors in each path which are both mounted on one translation stage (Newport 9066-COM-E-M), positioned with a stepper-motor (Newport

8301NF, with controller Newport 8743-CL).

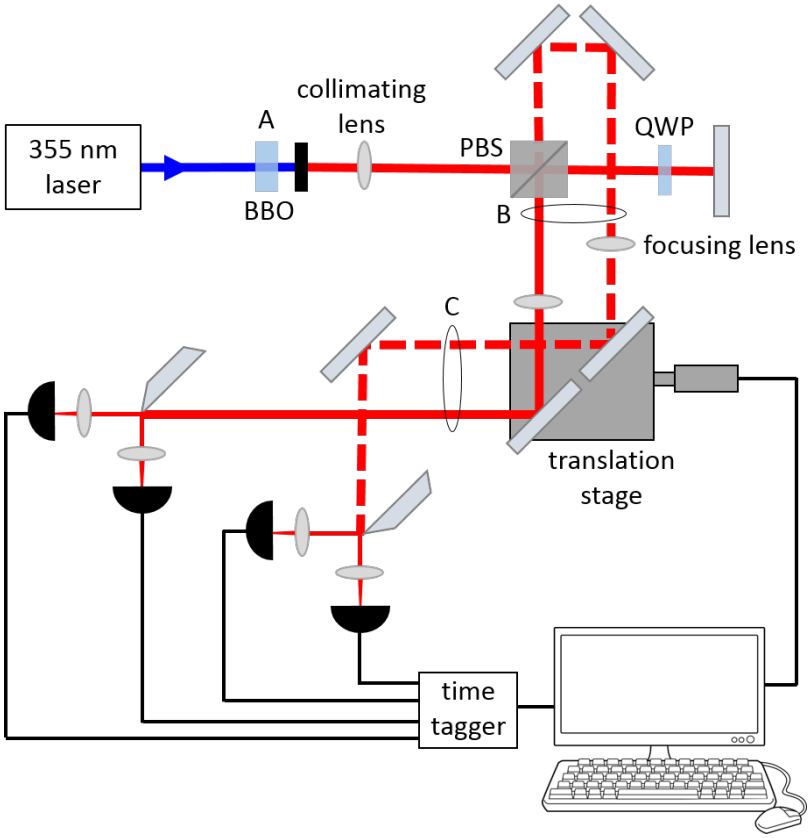

(a)

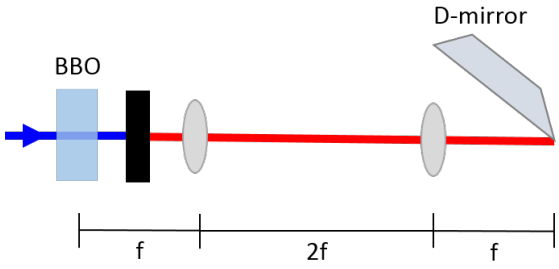

(b)

Figure 5.2: (a) Our setup for using spatial correlations between entangled photons in a displacement measurement. A 355-nm laser pumps a BBO crystal producing 2 photons with orthogonal polarization in the same direction. They are then split by the PBS into two separate paths; one path flips the x-coordinates while the other does not. Two mirrors both mounted on a translation stage control displace the photons by the same amount. Three lenses image the spatial profile in the crystal to two position detectors, each consisting of a D-mirror (in the image plane) that reflects half of the incident beam toward one detector and transmits the rest toward the other detector. Coincidences between the four detectors are analyzed to determine the beam displacement. The theoretical position joint-probability distribution at the points marked A, B, and C are shown in Fig. 5.1. (b) A simplified schematic showing 4f-imaging of the BBO crystal onto the D-mirrors of the position-measurement system.

After interacting with the displacing mirror, each photon is split into left and right 'halves' by a D-

shaped mirror (Thorlabs BBD1-E02) and is detected by one of two APD's (we have a total of four APD's; 3 are Perkin Elmer model SPCM-AQR-13 and 1 is Perkin Elmer SPCM-CD 2801). (To measure the joint-probability distribution, the D-mirrors are replaced with 5-μm wide slits (Thorlabs S5RD).) Each path contains a another 175-mm focal-length lens positioned 350 mm from the first lens and 175 mm from the D-shaped mirrors, so that the spatial profile in the crystal is imaged onto the position detector. Note that the displacing mirror is placed after the focusing lenses.

After detection, each APD pulse is analyzed with a timetagger (Universal Quantum Devices model Logic16) and the arrival time of each photon is recorded. Beam displacements are determined by recording 1 continuous second of timetags at each motor position. From this data, we then determine when coincidences occurred within a 4 ns window between the four pairs of detectors, and then bin coincidences into 200 5-ms bins. This time-scale was chosen because it placed us well within the range where the coincidence counts were shot-noise limited, meaning we eliminated any noise from drift. From these 200 'trials', we obtain the average displacement (from Eqn. (5.1)) and the variance (from $\sigma^2_{var} = \frac{\sum_{i=1}^{200}(x_i - \bar{x})^2}{199}$). To eliminate any slippage or backlash in the motor or translation stage as we move between points, we always start from a position of -100 units, move to zero units, and then to the measurement position (or to the measurement position and then zero, depending on which was smaller), taking a similar data set at 0 units. The average position at 0 units was subtracted from the average measurement position. The motor was calibrated to find that the motor moves 74.6 nm per unit.

5.3 Results and Discussion

Our results are shown in Figs. 5.3 - 5.8. Fig. 5.3 shows the result of scanning with 5-μm slits to obtain the full 2D distribution, to give a sense of scale. Fig. 5.4 shows the profile for each crystal, obtained by integrating across the x_+ and x_- directions. Here it becomes clear that our Gaussian approximation (Eqn. (4.13)) is indeed just an approximation, and especially in the case of the narrow x_+ profile, the Gaussian fit fails to correctly capture the wings of the distribution. From our fit, we obtained $\sigma_+ = 4$ μm (with a measured FWHM = 18.4 μm) for the 1-mm crystal and $\sigma_+ = 9.6$ μm (measured FWHM = 31.1 μm) for the 3-mm crystal. From Eqn. (4.16), we estimate that for the 1-mm (3-mm) crystal, $\sigma_+ = 5.0$ μm (8.7 μm), in good agreement with our measurement. In the wide x_- direction, we see that it fits well across most of the distribution, and the fit values of $\sigma_- = 346$ μm (1-mm crystal) and $\sigma_- = 358$ μm (3-mm crystal) agree reasonably well with our measured pump width $\sigma_p = 286$ μm (which ideally would imply $\sigma_- = 404$ μm). We expect some deviation from theory, since our distributions are not truly Gaussian.

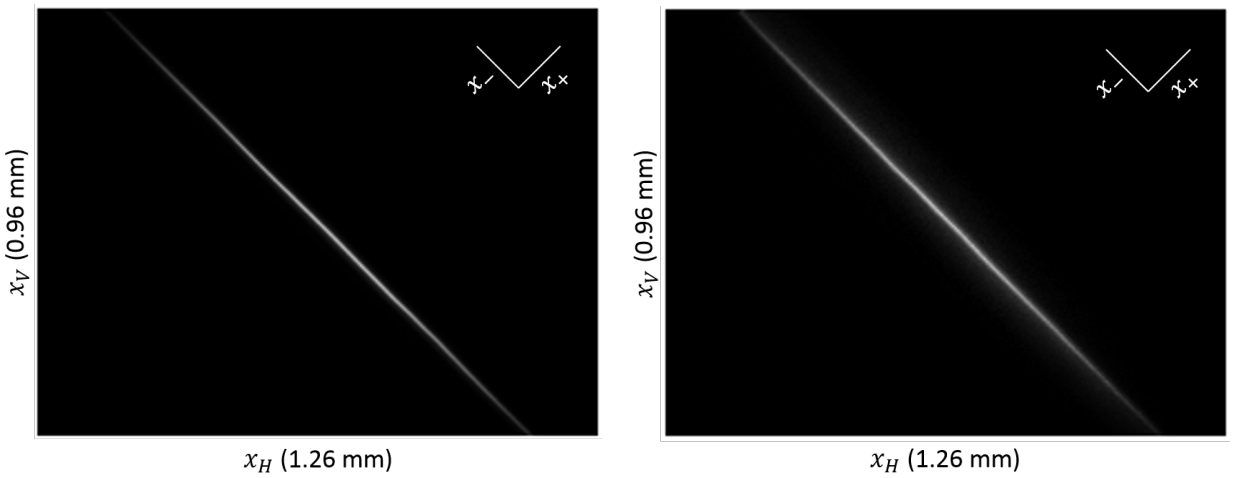

(a) (b)

Figure 5.3: The full position joint probability distribution for the (a) 1-mm and (b) 3-mm long crystals. Note that, as expected, the spatial correlations are tighter (i.e. the narrow axis is smaller for the shorter crystal, since the momentum correlations are weaker) in the 1-mm long crystal.

Fig. 5.5 shows the measured shift compared to the calibrated shift of the picomotor over the full width of σ_-. It saturates when the shift becomes approximately as large as σ_-. Interestingly, we notice that the measurement gives a useful result even in the range of shifts between σ_+ and σ_-. The deflection signal from a classical uncorrelated beam of width σ_+ would saturate for shifts bigger than σ_+ (as the beam would be entirely to one side of the split detector), which shows that correlated photons offer not only improved resolution with a large beam, but over an increased range.

Fig. 5.6 shows the measured shift compared to the calibrated picomotor shift for $d < \sigma_+$ (the near-zero region) and for $\sigma_+ < d < \sigma_-$ (the intermediate region). A model [1] of displacements in both regions showed that the slope should be constant and equal to 1 across both. For the near-zero region, we measured slopes of 0.92 ± 0.04 and 0.58 ± 0.01 for the 1-mm and 3-mm crystals, respectively, and in the intermediate region we measured 0.83 ± 0.01 and 0.982 ± 0.003. Our model also showed that a spatially dependent loss [2], such as might come from light scattering off the edge of the D-mirrors, could cause the slope to be smaller than 1. If we model a 5-μm edge that scattered 100% of incident light, our model showed slopes of 0.64 and 0.96 in the near-zero region for the 1-mm and 3-mm distributions, respectively, and 0.96 and 0.88 in the intermediate region. We also tried to estimate the thickness of the edge by placing the D-mirror in the middle of a laser beam and attributing any loss from scattering on the edge (namely, 1-R-T). Our measurement was consistent with each mirror having an edge of about 10 μm. We therefore think it is likely that the discrepancy is

[1] We modeled the signal we might expect from our measured distribution by separating the image matrix in Fig. 5.3 into four quandrants numerically depending on the amplitude of the 'applied shift'.

[2] We modeled a spatially-dependent loss by subtracting out rows and columns from the image matrix that represent where the 'D-mirror edge' would be located.

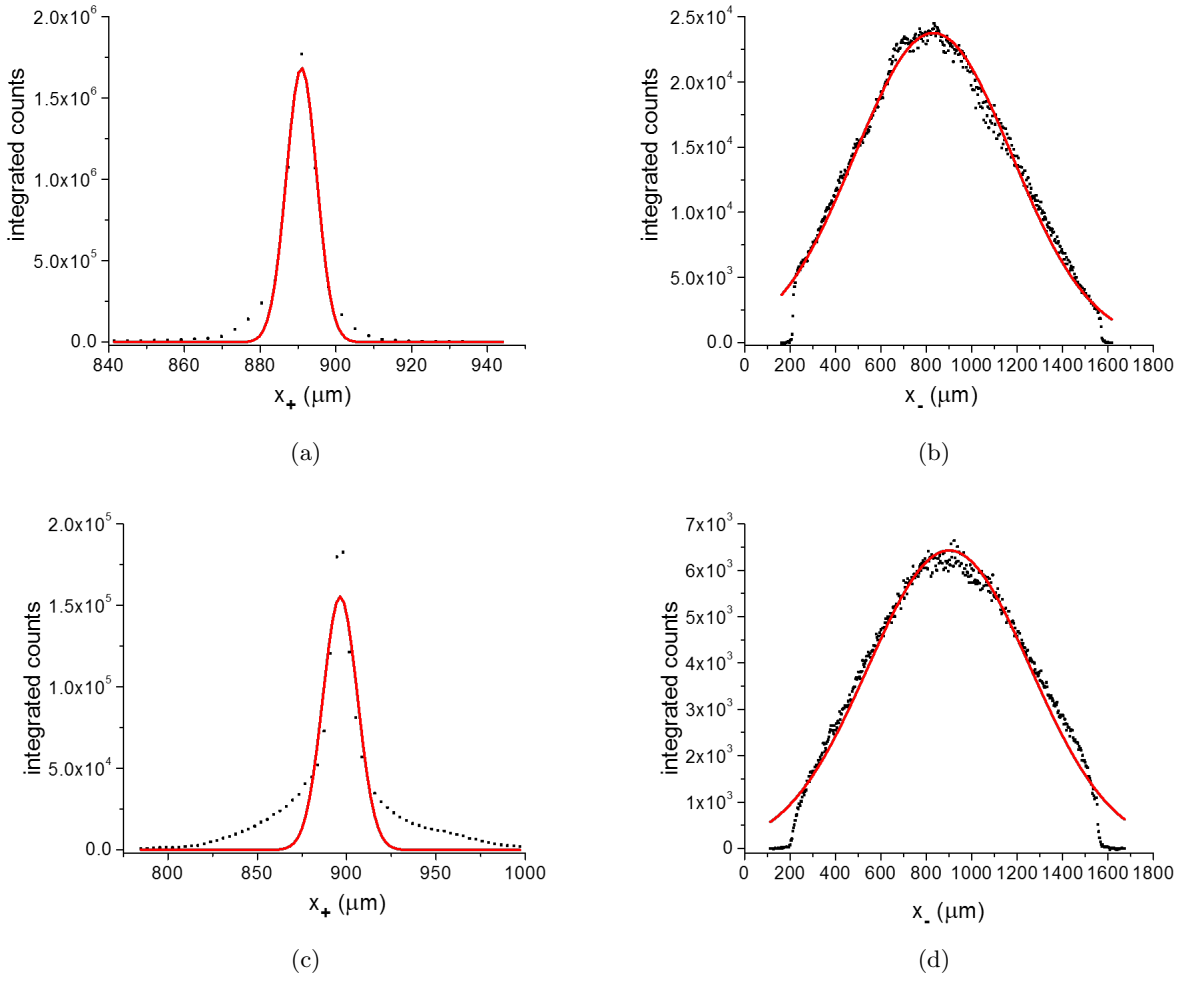

(a) (b)

(c) (d)

Figure 5.4: The measured 1-D profiles (black squares) along the x_+ and x_- directions for the 1-mm ((a) and (b)) and 3-mm long ((c) and (d)) crystals. The red lines show the fit Gaussian distribution. (a) gives $\sigma_+ = 4$ μm, (b) gives $\sigma_- = 346$ μm, (c) gives $\sigma_+ = 9.6$ μm, (d) gives $\sigma_- = 358$ μm.

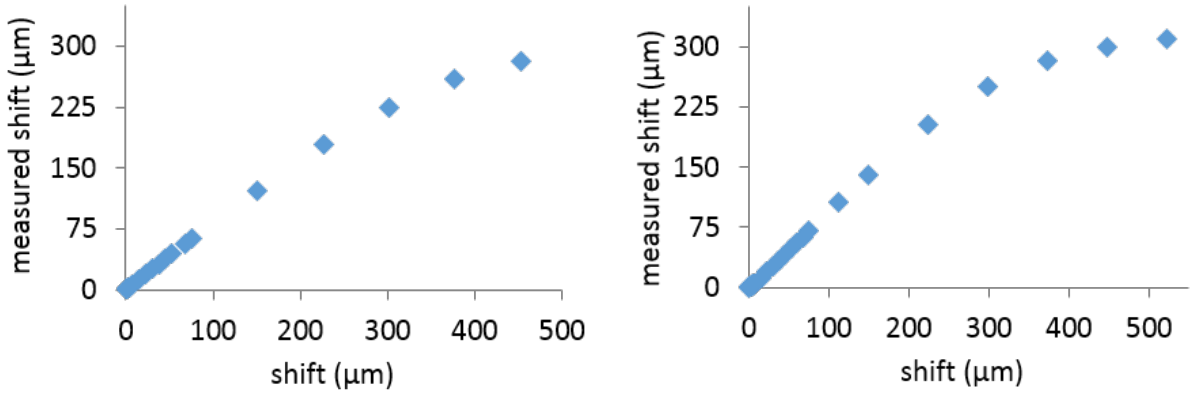

(a) (b)

Figure 5.5: The measured shift versus the applied shift. The signal begins to saturate around applied shifts = σ_-, when the entire 2-D distribution is contained in the upper right quadrant. Notice that for shifts between σ_+ and σ_-, the signal increases linearly, which would not be the case for a classical beam of width σ_+.

caused by scattering from the edges of the mirrors[3].

Fig. 5.7 shows the measured variance in the same four cases along with theoretical predictions from [24]. We note that in the near-zero region, the variance is constant, as one would expect for a shot-noise limited measurement with roughly the same number of photons on each side of the split-detector (as is the case for small displacements). In the intermediate region, however, notice that the variance increases linearly with displacement. This happens because the shift in the distribution is large enough that it lies entirely in the RR quadrant (since we have plotted + shifts), and a larger shift actually pulls a larger fraction of the entire distribution into the RR quadrant, while the LL quadrant has no photons. That causes the total number of coincidence counts in the numerator of Eqn. (5.1) to increase and the variance to correspondingly increase.

From our measurements in the near-zero region, we calculated the average measured standard deviation per-coincidence. For the 1-mm (3-mm) crystal we observed 63 μm (58 μm). Our expected values were 26 μm (41 μm), which is quite different than our measured values. We think this is likely also caused by scattering on the D-mirror edges, since our model and displacement data are consistent with an edge around 5-10 μm, which is about the same size as σ_+. This would imply that for small displacements, nearly the entire center of the distribution would be attenuated and most of the coincidences on the detector would come from the wider wings of the distribution, causing it to look broader and consequently increasing our measured variance. The variance matches theory more closely in the intermediate region, when the edge is far from the brightest part of the distribution. For the largest shifts in the intermediate region the measured

[3]Our model did not capture the behavior of the 1-mm distribution, which was larger in the near-zero region than in the intermediate region. This may be because with 5-μm pixels it is difficult to model shifts less than 5 m. It would be ideal to repeat this analysis with a more sophisticated model with smaller pixels.

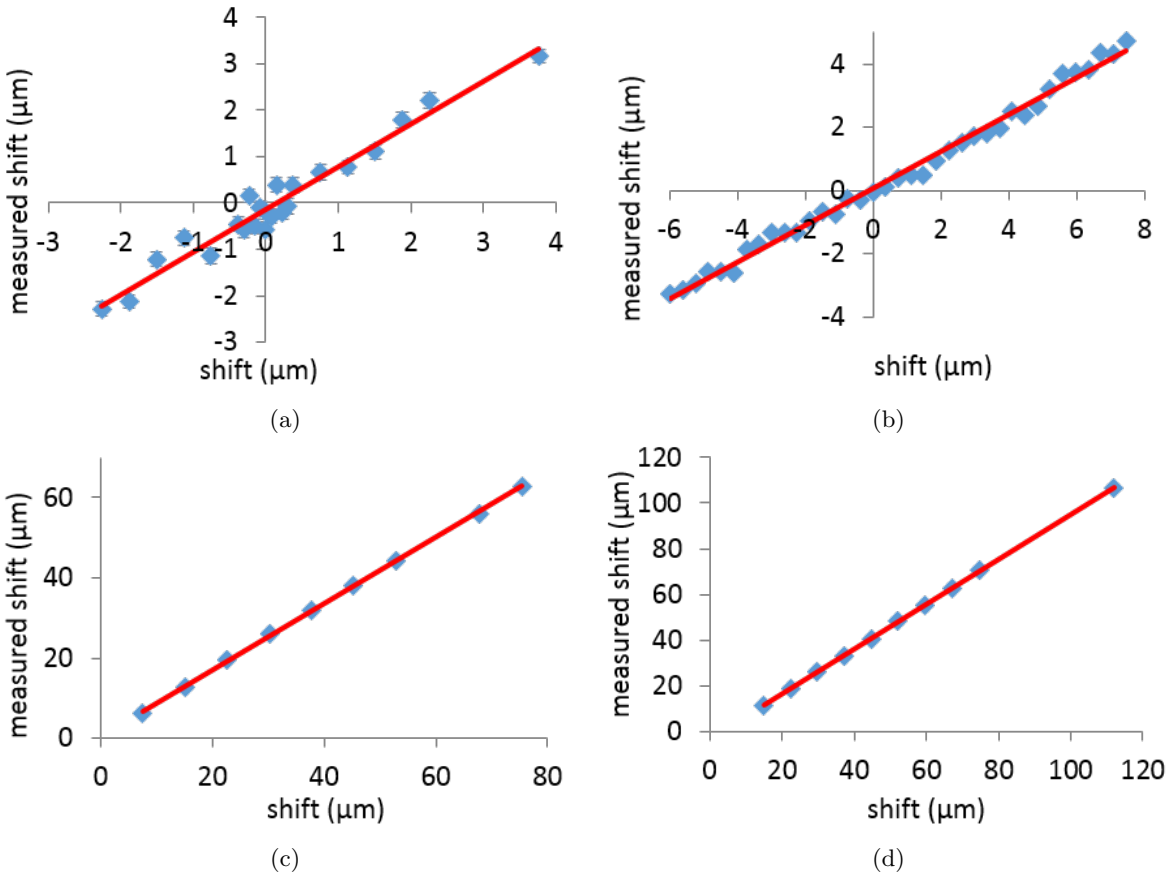

Figure 5.6: The measured shift versus the applied shift (blue diamonds) in the near-zero ((a) 1-mm long crystal, (b) 3-mm long crystal) and intermediate regions ((c) 1-mm long crystal, (d) 3-mm long crystal). We expected the slope to be 1 in all cases. Red lines show the linear fits with values: (a) 0.92 ± 0.04, (b) 0.58 ± 0.01, (c) 0.83 ± 0.01, (d) 0.982 ± 0.003. The discrepancy is probably caused by spatially dependent loss in the position-detector, for example scattering from the edge of the D-mirror. Note that the signal increases linearly even in the intermediate region, which for a classical beam of width σ_+ would show a saturated signal.

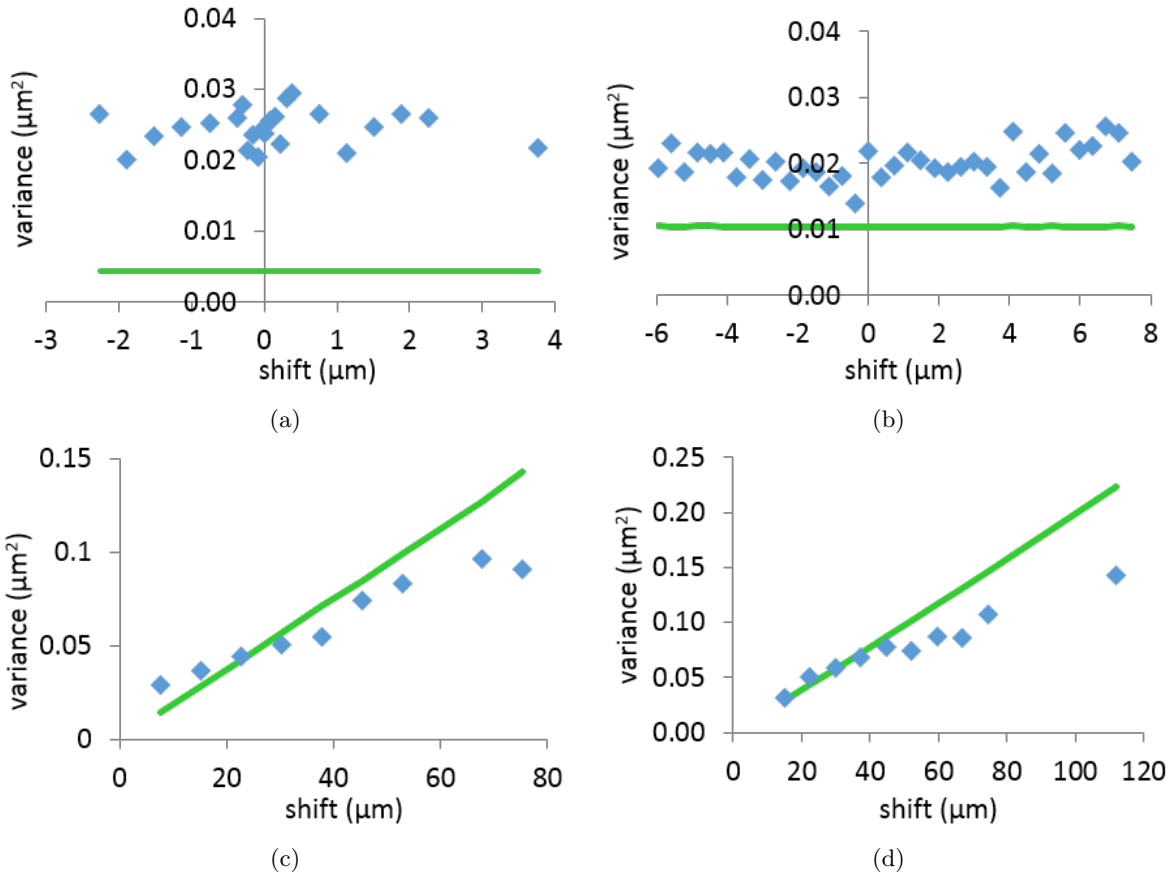

Figure 5.7: The measured variance (blue diamonds) versus the applied shift in the near-zero ((a) 1-mm long crystal, (b) 3-mm long crystal) and intermediate regions ((c) 1-mm long crystal, (d) 3-mm long crystal). Light green lines show the expected variance from theory. Notice that in the near-zero region, the variance is flat, as expected, since the counts in the upper right and lower left are roughly equal. In the intermediate region, the variance increases linearly as more counts are pulled into the upper right quadrant for progressively larger shifts.

variance does deviate from theory, perhaps because the approximation $d < \sigma_-$ is less valid there.

Fig. 5.8 shows the measured SNR for the previous four cases, plotted along with theory and with the expected SNR for a classical uncorrelated beam with $\sigma = \sigma_-$. In the near-zero region, we measured average SNR increases of 6.4 ± 0.3 and 7.68 ± 0.07 for the 1-mm and 3-mm crystals, respectively. Our measured SNR is consistently smaller than theory, because our variance is larger and our signal is smaller, as we discussed. Note that our measured SNR is also consistently bigger than for a classical beam of width $\sigma = \sigma_-$, demonstrating an improvement with SPDC correlations. In the intermediate region we measured 2.5 ± 0.2 and 2.8 ± 0.2. Again, our SNR agrees better with theory in this region, as the D-mirror edge is far from the center of the distribution.

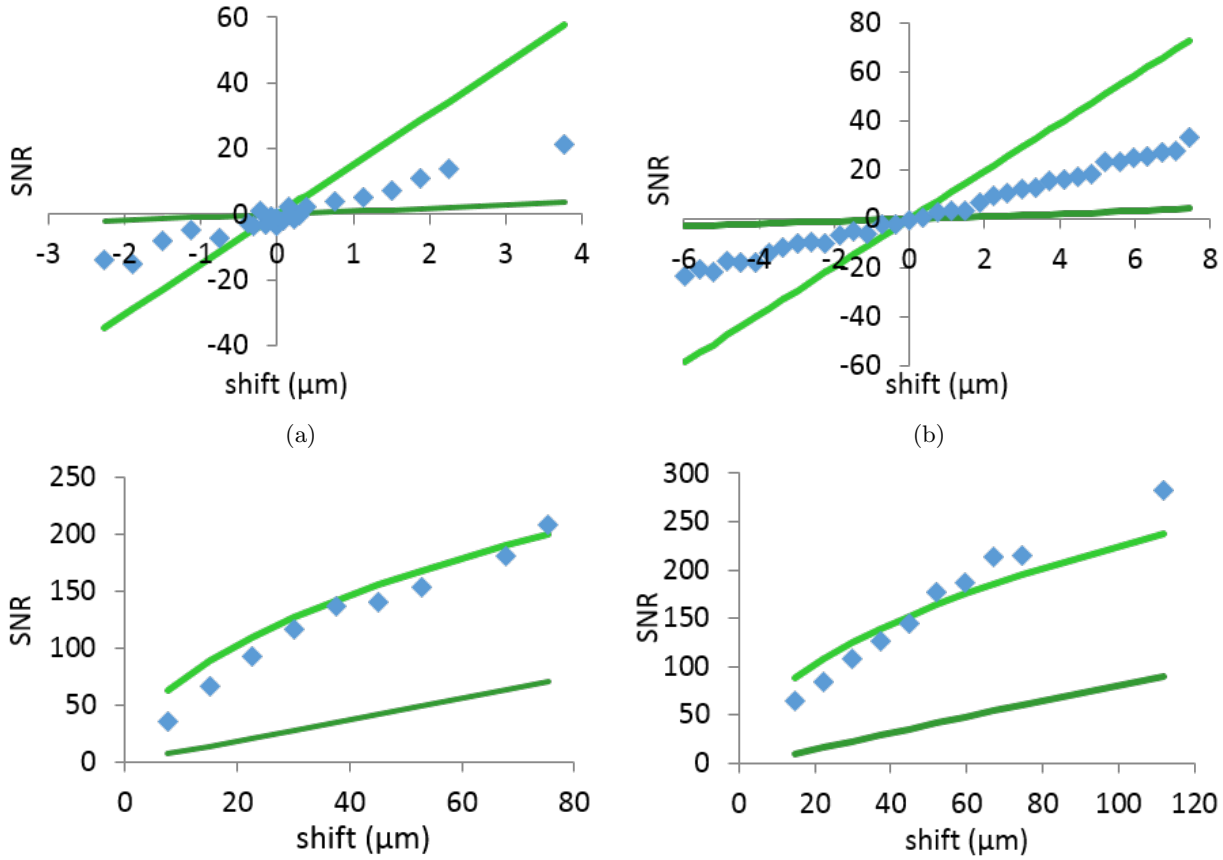

Figure 5.8: The measured SNR versus the applied shift (blue diamonds) in the near-zero ((a) 1-mm long crystal, (b) 3-mm long crystal) and intermediate regions ((c) 1-mm long crystal, (d) 3-mm long crystal). Light green lines show the expected SNR from theory. Dark green lines show the expected SNR for a classical beam of width σ_{-}.

Chapter 6

Attempting to Use a Quantum Eraser to Improve AFM Sensitivity

6.1 Atomic Force Microscopy and Quantum Erasure

An atomic force microscope (AFM) uses a cantilever with an atomic-scale tip to probe the surface of a material. The flexible tip deforms when in contact with a surface, causing light incident on the side of the tip to be reflected in different directions. By detecting the difference in reflections between a relaxed and flexed cantilever, the surface can be mapped.

Magnetic resonance force microscopy (MRFM) is a variant of AFM that detects the force exerted by electron spins in a magnetic field gradient. It was developed to image materials on the atomic scale with chemical specificity. This technique could enable the structure of proteins, viruses, and other complicated materials to be determined in a novel manner. MRFM has already been used for 3-dimensional proton-spin tomography with 10-nm resolution [25]. A breakthrough in MRFM technology came from the development of silicon nanowire mechanical oscillators, which have low intrinsic energy dissipation. Experiments at the University of Illinois previously demonstrated MRFM experiments utilizing silicon nanowire oscillators to detect thermal-force-noise-limited spin detection of proton spins and Fourier-transform magnetic resonance imaging of proton spins [26] with 10-nm spatial resolution [27].

The displacement of a silicon nanowire cantilever is measured using a fiber optic interferometer, as shown in Fig. 6.1(a). Light is coupled through a polarization-maintaining fiber and a cleaved tip is placed close to the cantilever such that a small amount of light reflects from the cantilever back into the fiber. Reflection from the tip of the fiber interferes with light from the cantilever at the input-end of the fiber.

Several factors limit the resolution of the fiber-AFM interferometer. First, light incident on the cantilever causes heating, so the number of photons that can interact with it is limited. Second, the diameter of the silicon nanowire is only 50 nm, so only about 1% of incident light is reflected from and coupled back into the fiber. A method of controlling the reflection from the fiber tip was not designed into the system, and it is much greater than the 1% from the cantilever. This causes the visibility of the interference fringes to be small and making changes in the cantilever position harder to discern.

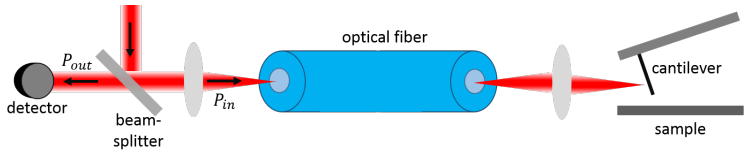

(a)

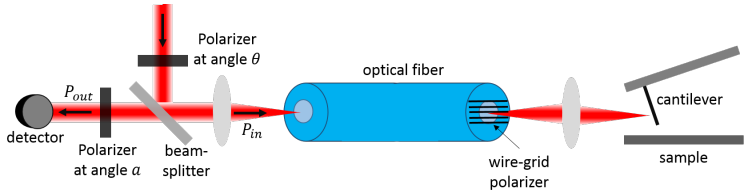

(b)

Figure 6.1: (a) The setup for sensing with an AFM. Light is coupled through a polarization maintaining fiber. Some reflects off the end of the fiber, while some is reflected from the cantilever back into the fiber. Interference fringes observed at the output are used to determine the cantilever displacement. (b) The proposed setup for combining an AFM with a quantum eraser. A wire-grid polarizer is printed on the end of the fiber, so that H is reflected while V is transmited. A PBS placed at the output allows the relative amplitude from the fiber end and the cantilever to be chosen to maximize the fringe visibility.

We sought to develop a straightforward method for controlling the relative intensity of the two interferometer paths, using a method called quantum erasure. It has long been known that any which-path information allowing two particles or interferometer paths to be distinguishable causes a reduction in the visibility of interference fringes. In the AFM setup, the differing reflection amplitudes provides such which-path information, as any photon returning to the detector is most likely reflected from the fiber end. In a quantum eraser (QE) experiment, which-path information is discarded, recovering indistinguishability. The idea is to mark the interferometer path with polarization, with V hitting the cantilever (since that maximizes it reflection from the narrow tip), and H hitting the fiber end. At the output, we place a polarizer whose orientation would determine the amplitude from each path at the detector; by discarding most of the light reflected from the fiber tip and equalizing these amplitudes, we can recover full visibility fringes.

As we will show below, we found that while the QE technique *did* offer some improvement in sensitivity, it was marginal enough that it was not worth the effort of installing it into a real system.

6.2 Setup and SNR

As shown in the figure, the AFM we consider works by placing the end of a fiber close to an oscillating cantilever. By interfering light reflected from the end of the fiber and from the cantilever, the displacement of the cantilever can be determined. In the original design, the visibility of the fringes is determined by the reflectivities of the fiber end and cantilever. We will compare this case to the case using a quantum eraser,

shown in Fig. 6.1(b), in which a wire-grid polarizer would be coated on the fiber end to transmit V and reflect H. At the output, another polarizer would be placed to control the analysis angle.

The interference fringes in the output power in all cases will be of the form

$$P = A + B\cos\phi \propto (1 + V\cos\phi), \tag{6.1}$$

where ϕ is the phase induced by the displacement of the cantilever and the the visibilty $V \equiv \frac{P_{max}-P_{min}}{P_{max}+P_{min}} = \frac{B}{A}$. We will operate around $\phi = \frac{\pi}{2}$ (the optimal value is slightly shifted from $\frac{\pi}{2}$, but it doesn't change our results). Then for a small shift in ϕ, the change in the power will be approximately $B\Delta\phi$, which is our signal. We consider the case that we are limited by the quantum shot-noise of the detected light; hence, the noise will be proportional to the square root of the detected power (which is approximately A). Our SNR is then

$$SNR_{QE} = \frac{B\Delta\phi}{\sqrt{A}}. \tag{6.2}$$

6.3 Without Polarization Quantum Eraser

The original design of the AFM is such that approximately 5% of the input power (P_{in}) is reflected off the end of the fiber. The cantilever reflects about 1% of the input power back into the fiber. Then the measured power will be

$$P_{out} = |\sqrt{P_{in}}(\sqrt{.05} + \sqrt{.01}e^{i\phi})|^2 = P_{in}(0.06 + 0.045\cos\phi), \tag{6.3}$$

leading to

$$SNR_{wo} = 0.045\sqrt{\frac{P_{in}}{0.06}}. \tag{6.4}$$

6.4 With Polarization Quantum Eraser

We send in the state

$$\sqrt{P_{in}}(\cos\theta|H\rangle + \sin\theta|V\rangle). \tag{6.5}$$

Assuming a polarizer perfectly reflective for $|H\rangle$ and perfectly transmissive for $|V\rangle$, this evolves to

$$\sqrt{P_{in}}(\cos\theta|H\rangle + e^{i\phi}\sqrt{.01}\sin\theta|V\rangle) \tag{6.6}$$

after reaching the fiber end. At the output, the light then passes through a polarizer at angle α, leaving the photons in the state

$$|\alpha\rangle\sqrt{P_{in}}(\cos\theta\cos\alpha + e^{i\phi}\sqrt{.01}\sin\theta\sin\alpha), \tag{6.7}$$

with a corresponding output power of

$$P_{out} = P_{in}(\cos^2\theta\cos^2\alpha + 0.01\sin^2\theta\sin^2\alpha + 2\cos\phi * 0.10\cos\theta\cos\alpha\sin\theta\sin\alpha). \tag{6.8}$$

From this we have

$$SNR_w = 0.20\cos\theta\cos\alpha\sin\theta\sin\alpha\sqrt{\frac{P_{in}}{\cos^2\theta\cos^2\alpha + 0.01\sin^2\theta\sin^2\alpha}}. \tag{6.9}$$

6.5 Comparison of the Two Cases

As mentioned above, the desirable power incident on the cantilever (P_c) is limited by heating effects. Thus, our P_{in} in each case will be determined by P_c. For the case *without the quantum eraser* $P_{in,wo} = \frac{P_c}{0.01}$; for the case *with the quantum eraser* $P_{in,QE} = \frac{P_c}{0.01\sin^2\theta}$. For comparison, we set $P_c = 1$.

Plugging our values for P_{in} into the above expressions, we obtain

$$SNR_{wo} = 1.84. \tag{6.10}$$

For the case with the quantum eraser, we optimize θ and α (using Mathematica), finding the largest value

$$SNR_{QE} = 2 \tag{6.11}$$

for $\theta = 0$ and $\alpha = \frac{\pi}{2}$ (i.e., send in as many H photons as possible to increase the output power, but keep most of the V photons from the cantilever). Note that the SNR values we have found here are not independently meaningful, since we left them in terms of power instead of photon number. However, the ratio of the two is a valid measure of comparison. Hence, we have found that adding a quantum eraser *would* improve the SNR, but only marginally in this situation. It might seem surprising that the QE doesn't lead to a greater advantage. The reason is that the visibility in the original version is actually already quite high:

$V_{wo} = \frac{(\sqrt{0.05}-\sqrt{0.01})^2}{(\sqrt{0.05}+\sqrt{0.01})^2} = 0.74$

6.6 Relation to a Typical Local Oscillator

If we tried to beat our small signal with a large local oscillator, our output signal would look like

$$|E_{LO} + e^{i\phi}E_c|^2 = E_{LO}^2 + E_c^2 + 2\cos\phi * E_{LO}E_c \tag{6.12}$$

where E_{LO} is the amplitude of the local oscillator field and similarly for E_c. Then the SNR is

$$\frac{2E_{LO}E_c}{\sqrt{E_{LO}^2 + E_c^2}}. \tag{6.13}$$

In the limit that $E_{LO} >> E_c$, then $SNR = 2E_c \approx 2\sqrt{P_c}$, as we found above in Eqn. (6.11).

Chapter 7

Conclusions

We have presented our exploration of ways to beat the standard quantum limit in deflection and displacement measurements. We showed that weak measurements combined with recycling offer an increased resolution in determining a mirror deflection over the conventional method by increasing the number of detected photons. Using recycling, we demonstrated an increase in the SNR by a factor of 2 over a single-pass WM. Though we were unable to demonstrate experimentally that recycling improved the SNR compared to conventional methods, we think our results show the logical extreme for weak measurements and demonstrate their potential in certain cases.

Using spatial correlations from SPDC, we showed that the uncertainty in a beam displacement measurement can be much smaller than the beam width, a nonclassical effect. The resolution is ultimately limited by the length of the SPDC crystal; a smaller crystal allows greater uncertainty in the relative momentum distributions of the correlated photons, with a corresponding reduction in the relative spatial uncertainty. We also showed that in the case of a split-detection measurement, coincidence detection allows an increased dynamic range even with a small beam.

Finally, we wanted to use a QE to improve the sensitivity of an AFM by increasing the interference fringe visibility, but found theoretically that equalizing the intensity in the interferometer arms only offered a modest boost. Nevertheless, there may be applications where the enhancement from intensity equalization is large enough to warrant the extra experimental complexity.

Appendix A

Aligning the 4-f Imaging Sytem for Recycling

Here we discuss in detail how we set up the 4-f imaging for the weak measurement recycling setup. A 4-f system is the ideal system for our purposes, because properly aligned, it should produce exactly the same beam on every pass. We can see this by examining the ABCD matrix of a 4-f imaging system (for more detail see [28], Chapters 1 and 3):

$$\begin{bmatrix} 1 & f \\ 0 & 1 \end{bmatrix} \begin{bmatrix} 1 & 0 \\ \frac{-1}{f} & 1 \end{bmatrix} \begin{bmatrix} 1 & 2f \\ 0 & 1 \end{bmatrix} \begin{bmatrix} 1 & 0 \\ \frac{-1}{f} & 1 \end{bmatrix} \begin{bmatrix} 1 & f \\ 0 & 1 \end{bmatrix} = - \begin{bmatrix} 1 & 0 \\ 0 & 1 \end{bmatrix}. \tag{A.1}$$

Starting from the tilting mirror in Fig. A.1(a), and shown with the loop unfolded in Fig. A.1(b), this represents the beam propagating 0.3 m, propagating through a lens with f = 0.3 m, propagating 0.6 m through the Pockels cell loop, transmitting through the lens again, and propagating back to the tilting mirror. When combined with the rest of our system (which has a total of 8 reflections with 2 focal points), we get the identity matrix, implying that our beam should be identical on every pass.

We aimed to place the tilting mirror at the focal point in an attempt to make our measurements with a collimated beam, and also to create another focal point near the Pockels cell, so the k-vector content is the same across the beam. To actually align the system. we first placed a microscope objective and zoom-beam-expander at the output of our single-mode fiber, as shown in Fig A.1(a). We adjusted the positions of the two until the waist location was about 0.5 m from the beam, or about the distance from the beam expander to the mid-point of the PC loop, which we confirmed by measuring the beam size as a function of distance from the beam expander, shown in Fig. A.2(a). We then placed the 4-f lens approximately 0.3 m from the mid-point of the Pockels cell loop and measured the waist size as a function of distance from the 4-f lens, shown in Fig. A.2, to confirm that the focal point was 0.3 m away, as we did observe.

In order for the 4-f system to work properly, the length of the PC loop and WM interferometer loop must be nearly equal to 2f, or 0.6 m, to within a few hundred micrometers. Because it is practically impossible to measure such a distance that precisely by hand, especially when multiple reflections are included, we instead mounted the 4-f lens and two of the PC-loop mirrors on translation stages. Adjusting the 4-f lens allowed

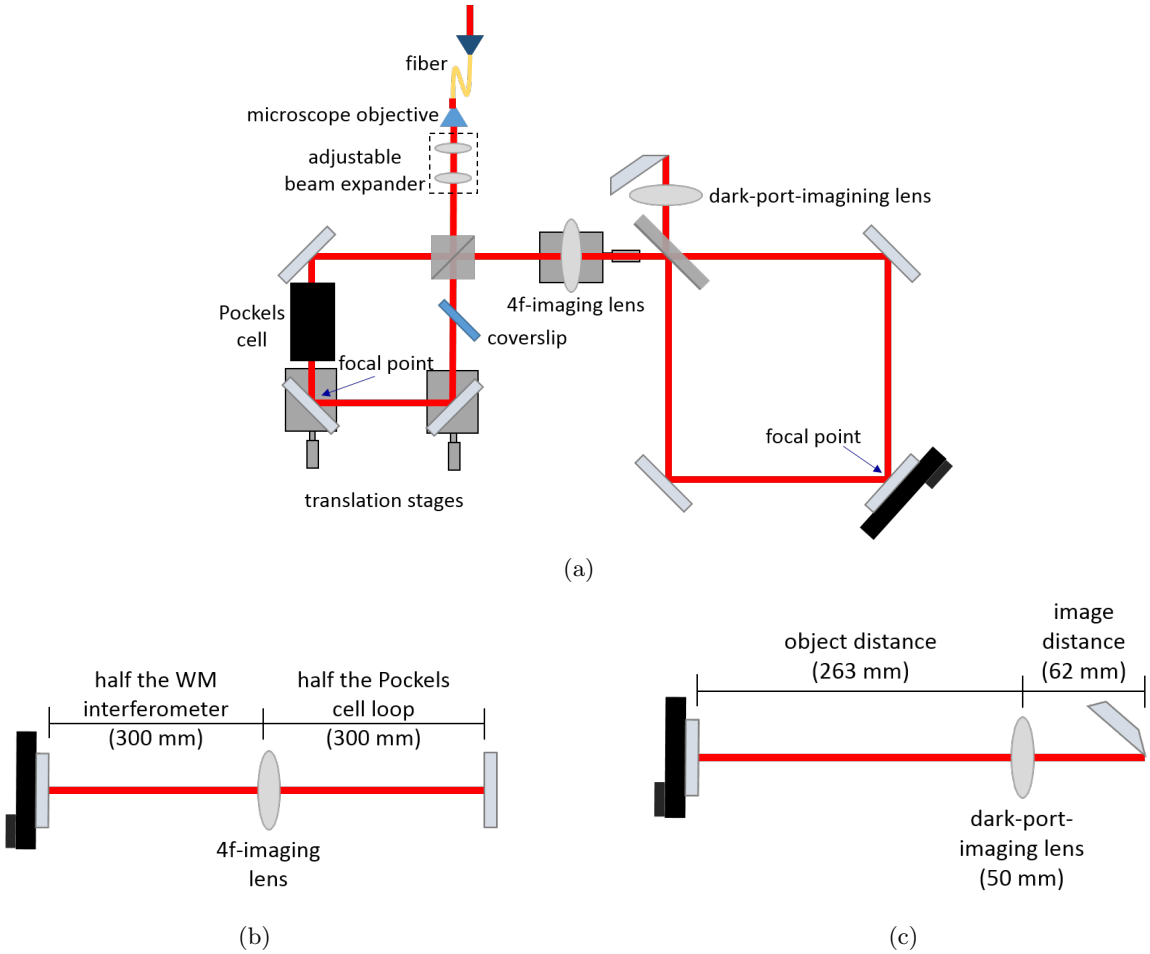

Figure A.1: (a) The 4-f imaging system implement into the recycling setup. The 4-f lens and two mirrors in the PC loop were mounted with translation stages to enable fine tuning of the length of the PC loop and WM-interferometer loop. (b) The 4-f imaging system unfolded. (c) The dark-port imaging system unfolded.

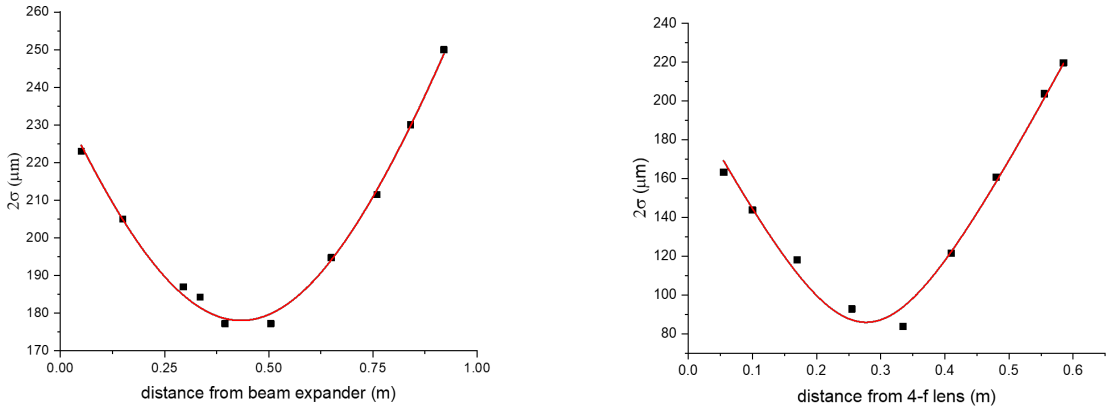

(a) (b)

Figure A.2: (a) The beam size as a function of distance from the adjustable beam expander. The position of the microscope objective was tweaked until the waist was located about 0.5 m from the beam expander, near the mid-point of the PC loop. (b) The beam size as a function of distance from the 4-f lens. The waist is approximately 0.3 m away, near the location of the tilting mirror.

us to change the length of the WM-interferometer loop, while adjusting the mirrors allowed us to change the length of the PC loop.

The positions of the translation stages were determined through trial-and-error, by monitoring the size of the beam in the dark port as a function of pass number. To find the size of the beam, we performed a time-resolved knife-edge scan by measuring the counts transmitted to an APD [1] as a function of the position of the D-mirror in the dark port, analyzing the arrival time with a timetagger, and fitting the output from each pass to an error-function. A representative result is shown in Fig. A.3(a).

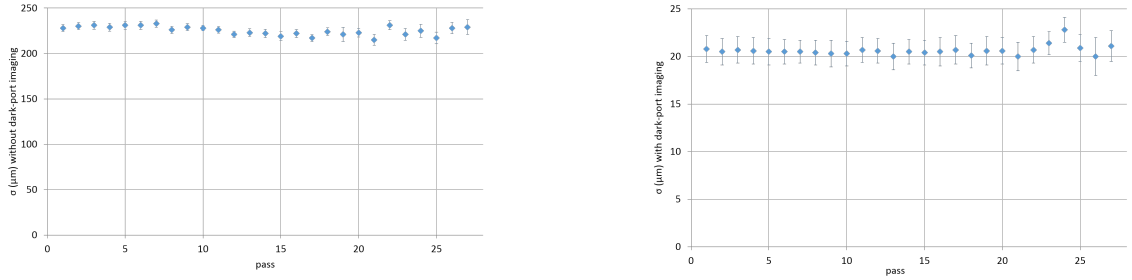

(a) (b)

Figure A.3: (a) The size of the beam at the dark-port position detector versus pass number. The beam size varies by at most a few percent over 27 passes. (b) The size of the beam at the dark-port position detector versus pass number after imaging the tilting mirror onto the position detector.

[1] The code used to record counts from each APD in the dark port can be found at: https://dx.doi.org/10.5281/zenodo.3340093, though it requires a MATLAB-timetagger interface library custom written for the Kwiat lab. The library is saved in the TimeTagger folder on the Desktop of my lab computer.

After aligning the 4-f system, we added another lens in the dark port in order to regain the optimal SNR, as discussed in Ch. 3. We used the thin lens equation $\frac{1}{o} + \frac{1}{i} = \frac{1}{f}$ to solve for o, the distance from the tilting mirror to the lens, and i, the distance from the lens to the position detector, for $f = 50.2$ mm and $o + i = 325$ mm (the distance from tilting mirror to detector). The dark-port imaging is shown unfolded in Fig. A.1(c). Another time-resolved knife-edge scan was performed; results are shown in Fig. A.3(b). When aligning the system with the full imaging setup, we found that we were not able to position the beam so that the D-mirror was precisely in the middle for each pass. We added a coverslip, as shown in Fig. A.1(a), and were able to properly align the system by tilting it a small amount.

Appendix B

Details of the Weak Measurement Data Analysis

Here we give a full description of the data-taking process for the weak measurement experiment.

The mirror is driven to oscillate at 500 Hz (period = 2 ms) at varying amplitudes. We collect counts for 300 s or 150,000 oscillation periods, giving us a 3-mHz resolution in frequency. Counts are collected from each APD, time-gated to keep only counts during the period a pulse cycles through the system, and then binned into 100-μs bins (so there are 20 bins per mirror oscillation period). We have an average of 2 counts per bin per detector.

After collecting and binning the raw counts, the difference between the left and right are taken for each time bin. Then, we perform the FFT at the oscillation frequency, take the absolute value, normalize by the total number of counts from the entire 300 s, mulitply by $\sqrt{\frac{\pi}{2}}$ (a normalization factor coming from the fact that our beam is Gaussian, as in [17]), and multiply by 4 to convert the FFT output to the peak-to-peak amplitude [1]. This process is repeated 20 times for each plotted data point in Fig. 3.7 and Fig 5.8.

The noise is calculated from similarly taking FFT of the counts difference, again normalized and scaled, but at 100 frequencies spaced 3 mHz from the oscillation frequency[2]. The noise is calculated from the root-mean-square, $\sigma_{noise} = \sqrt{\frac{\sum_i (d_i)^2}{99}}$. This is possible because the Poisson-distributed counts create a white noise across all frequencies, with each being independent of the others. It allows us to simultaneously gather many samples to compute the noise.

It is possible that by including only off-signal frequencies in our analysis, we miss some noise occuring only at the signal frequency, which may happen, for example, if the mirror or piezo itself has some extra uncertainty in the oscillation amplitude. To confirm that this was not the case, we took 100 repeated measurements with a 3 μrad peak-to-peak amplitude and took the standard deviation of those measurements. Our results were consistent with the expected standard deviation from shot-noise, so we concluded that it was the dominant effect.

[1] Our implementation of this algorithm can be found here https://zenodo.org/record/3340123.XS-ZhfJKipp
[2] Our code for this can also be found at the link above

References

[1] LIGO Scientific Collaboration and Virgo Collaboration, "Observation of gravitational waves from a binary black hole merger," *Phys. Rev. Lett.*, vol. 116, p. 061102, Feb 2016. [Online]. Available: https://link.aps.org/doi/10.1103/PhysRevLett.116.061102

[2] S. Fatayer, B. Schuler, W. Steurer, I. Scivetti, J. Repp, L. Gross, M. Persson, and G. Meyer, "Reorganization energy upon charging a single molecule on an insulator measured by atomic force microscopy," *Nature Nanotechnology*, vol. 13, p. 376380, May 2018.

[3] P. Dixon, D. Starling, A. Jordan, and J. C Howell, "Ultrasensitive beam deflection measurement via interferometric weak value amplification," *Phys. Rev. Lett.*, vol. 102, p. 173601, 06 2009.

[4] J. P. Dowling, "Quantum optical metrology – the lowdown on high-n00n states," 2009.

[5] R. J. Glauber, "Coherent and incoherent states of the radiation field," *Phys. Rev.*, vol. 131, pp. 2766–2788, Sep 1963. [Online]. Available: https://link.aps.org/doi/10.1103/PhysRev.131.2766

[6] G. A. Durkin and J. P. Dowling, "Local and global distinguishability in quantum interferometry," *Phys. Rev. Lett.*, vol. 99, p. 070801, Aug 2007. [Online]. Available: https://link.aps.org/doi/10.1103/PhysRevLett.99.070801

[7] C. M. Caves, "Quantum-mechanical noise in an interferometer," *Phys. Rev. D*, vol. 23, pp. 1693–1708, Apr 1981. [Online]. Available: https://link.aps.org/doi/10.1103/PhysRevD.23.1693

[8] T. Corbitt and N. Mavalvala, "Review: Quantum noise in gravitational-wave interferometers," *Journal of Optics B: Quantum and Semiclassical Optics*, vol. 6, July 2004. [Online]. Available: https://iopscience.iop.org/article/10.1088/1464-4266/6/8/008

[9] Y. Aharonov, D. Z. Albert, and L. Vaidman, "How the result of a measurement of a component of the spin of a spin-1/2 particle can turn out to be 100," *Phys. Rev. Lett.*, vol. 60, pp. 1351–1354, Apr 1988. [Online]. Available: https://link.aps.org/doi/10.1103/PhysRevLett.60.1351

[10] J. C. Howell, D. Starling, P. Dixon, P. Vudyasetu, and A. Jordan, "Interferometric weak value deflections: Quantum and classical treatments," *Phys. Rev. A*, vol. 81, 06 2009.

[11] A. J Leggett, "Comment on "how the result of a measurement of a component of the spin of a spin- z particle can turn out to be 100"," *Phys. Rev. Lett.*, vol. 62, p. 2325, 05 1989.

[12] I. M. Duck, P. M. Stevenson, and E. C. G. Sudarshan, "The sense in which a "weak measurement" of a spin-1/2 particle's spin component yields a value 100," *Phys. Rev. D*, vol. 40, pp. 2112–2117, Sep 1989. [Online]. Available: https://link.aps.org/doi/10.1103/PhysRevD.40.2112

[13] N. W. M. Ritchie, J. G. Story, and R. G. Hulet, "Realization of a measurement of a "weak value"," *Phys. Rev. Lett.*, vol. 66, pp. 1107–1110, Mar 1991. [Online]. Available: https://link.aps.org/doi/10.1103/PhysRevLett.66.1107

[14] G. I. Viza, J. Martínez-Rincón, G. B. Alves, A. N. Jordan, and J. C. Howell, "Experimentally quantifying the advantages of weak-value-based metrology," *Phys. Rev. A*, vol. 92, p. 032127, Sep 2015. [Online]. Available: https://link.aps.org/doi/10.1103/PhysRevA.92.032127

[15] D. J. Starling, P. B. Dixon, A. N. Jordan, and J. C. Howell, "Optimizing the signal-to-noise ratio of a beam-deflection measurement with interferometric weak values," *Phys. Rev. A*, vol. 80, p. 041803, Oct 2009. [Online]. Available: https://link.aps.org/doi/10.1103/PhysRevA.80.041803

[16] C. Ferrie and J. Combes, "Weak value amplification is suboptimal for estimation and detection," *Phys. Rev. Lett.*, vol. 112, p. 040406, Jan 2014. [Online]. Available: https://link.aps.org/doi/10.1103/PhysRevLett.112.040406

[17] S. Barnett, C. Fabre, and A. Matre, "Ultimate quantum limits for resolution of beam displacements," *The European Physical Journal D*, vol. 22, pp. 513–519, 03 2003.

[18] K. Lyons, J. Dressel, A. N. Jordan, J. C. Howell, and P. G. Kwiat, "Power-recycled weak-value-based metrology," *Phys. Rev. Lett.*, vol. 114, p. 170801, Apr 2015. [Online]. Available: https://link.aps.org/doi/10.1103/PhysRevLett.114.170801

[19] Y.-T. Wang, J.-S. Tang, G. Hu, J. Wang, S. Yu, Z.-Q. Zhou, Z.-D. Cheng, J.-S. Xu, S.-Z. Fang, Q.-L. Wu, C.-F. Li, and G.-C. Guo, "Experimental demonstration of higher precision weak-value-based metrology using power recycling," *Phys. Rev. Lett.*, vol. 117, p. 230801, Nov 2016. [Online]. Available: https://link.aps.org/doi/10.1103/PhysRevLett.117.230801

[20] J. Dressel, K. Lyons, A. N. Jordan, T. M. Graham, and P. G. Kwiat, "Strengthening weak-value amplification with recycled photons," *Phys. Rev. A*, vol. 88, p. 023821, Aug 2013. [Online]. Available: https://link.aps.org/doi/10.1103/PhysRevA.88.023821

[21] R. W. Boyd, *Nonlinear Optics, Third Edition*, 3rd ed. Orlando, FL, USA: Academic Press, Inc., 2008.

[22] N. A. Peters, "One- and two-photon states for quantum information," Ph.D. dissertation, University of Illinois at Urbana-Champaign, 2006.

[23] J. Schneeloch and J. C. Howell, "Introduction to the transverse spatial correlations in spontaneous parametric down-conversion through the biphoton birth zone," *Journal of Optics*, vol. 18, no. 5, p. 053501, apr 2016. [Online]. Available: https://doi.org/10.1088/2040-8978/18/5/053501

[24] K. Lyons, S. Pang, P. G. Kwiat, and A. N. Jordan, "Precision optical displacement measurements using biphotons," *Phys. Rev. A*, vol. 93, p. 043841, Apr 2016. [Online]. Available: https://link.aps.org/doi/10.1103/PhysRevA.93.043841

[25] C. L. Degen, M. Poggio, H. J. Mamin, C. T. Rettner, and D. Rugar, "Nanoscale magnetic resonance imaging," *Proceedings of the National Academy of Sciences*, vol. 106, no. 5, pp. 1313–1317, 2009. [Online]. Available: https://www.pnas.org/content/106/5/1313

[26] J. M. Nichol, E. R. Hemesath, L. J. Lauhon, and R. Budakian, "Nanomechanical detection of nuclear magnetic resonance using a silicon nanowire oscillator," *Phys. Rev. B*, vol. 85, p. 054414, Feb 2012. [Online]. Available: https://link.aps.org/doi/10.1103/PhysRevB.85.054414

[27] J. M. Nichol, T. R. Naibert, E. R. Hemesath, L. J. Lauhon, and R. Budakian, "Nanoscale fourier-transform magnetic resonance imaging," *Phys. Rev. X*, vol. 3, p. 031016, Sep 2013. [Online]. Available: https://link.aps.org/doi/10.1103/PhysRevX.3.031016

[28] B. E. A. Saleh and M. C. Teich, *Fundamentals of Photonics, Second Edition*, 2nd ed. Hoboken, NJ, USA: John Wiley and Sons, Inc., 2007.